WATER RESOURCES RESEARCH, VOL. 44, W05410, doi:10.1029/2008WR006858, 2008

Transport of conservative solutes in simulated fracture networks: 2. Ensemble solute transport and the correspondence to operator-stable limit distributions

Donald M. Reeves,[1] David A. Benson,[2] Mark M. Meerschaert,[3] and Hans-Peter Scheffler[4]

Received 28 March 2007; revised 14 January 2008; accepted 29 January 2008; published 15 May 2008.

[1] In networks where individual fracture lengths follow a fractal distribution, ensemble transport of conservative solute particles at the leading plume edge exhibit characteristics of operator-stable densities. These densities have, as their governing equations of transport, either fractional-order or integer-order advection-dispersion equations. Model selection depends on the identification of either multi-Gaussian or operator-stable transport regimes, which in turn depends on the power law exponent of the fracture length distribution. Low to moderately fractured networks with power law fracture length exponents less than or equal to 1.9 produce solute plumes that exhibit power law leading-edge concentration profiles and super-Fickian plume growth rates. For these network types, a multiscaling fractional advection-dispersion equation (MFADE) provides a model of multidimensional solute transport where different rates of power law particle motion are defined along multiple directions. The MFADE model is parameterized by a scaling matrix to describe the super-Fickian growth process, in which the eigenvectors correspond to primary fracture group orientations and the eigenvalues code fracture length and transmissivity. The approximation of particle clouds by a multi-Gaussian (a subset of the operator stable) for densely fractured networks with finite variance fracture length distributions can be ascribed to the classical ADE where Fickian scaling rates pertain along orthogonal plume growth directions. Fracture networks show long-term particle retention in low-velocity fractures so that coupling of the equations of motion with retention models such as continuous time random walk or multirate mobile/immobile will increase accuracy near the source. Particle arrival times at exit boundaries for multi-Gaussian plumes vary with spatial density. Generally, arrival times are faster in sparsely fractured domains where transport is governed by a few very long fractures.

Citation: Reeves, D. M., D. A. Benson, M. M. Meerschaert, and H.-P. Scheffler (2008), Transport of conservative solutes in simulated fracture networks: 2. Ensemble solute transport and the correspondence to operator-stable limit distributions, *Water Resour. Res.*, *44*, W05410, doi:10.1029/2008WR006858.

1. Introduction

[2] The use of an analytical solution to an equation such as the advection-dispersion equation (ADE) would be very convenient for screening-level predictions of solute transport in fractured media. Unfortunately, the ADE has been shown to be inadequate for describing solute transport behavior in sparsely to moderately fractured rock masses [*Schwartz et al.*, 1983; *Smith and Schwartz*, 1984; *Berkowitz and Scher*, 1997; *Becker and Shapiro*, 2000; *Painter et al.*, 2002; *Kosakowski*, 2004; *Zhang and Kang*, 2004; *Jiménez-Hornero et al.*, 2005]. At the network scale, non-Gaussian transport behavior may be partially explained by the fractal nature of fracture networks. The distribution of permeability and/or trace lengths of individual fractures or fracture zones can vary over several orders of magnitude [e.g., *Bour and Davy*, 1997; *Bonnet et al.*, 2001; *Stigsson et al.*, 2001; *Gustafson and Fransson*, 2005], resulting in highly heterogeneous flow fields where equivalent properties cannot be defined over a larger continuum [*Long et al.*, 1982]. Instead of converging to elliptical multidimensional Gaussian (multi-Gaussian) densities, transport of particles through a restricted subset of interconnected fractures can lead to highly asymmetric solute plumes with anomalous scaling rates [e.g., *Becker and Shapiro*, 2000; *Kosakowski*, 2004].

[1]Desert Research Institute, Reno, Nevada, USA.
[2]Department of Geology and Geological Engineering, Colorado School of Mines, Golden, Colorado, USA.
[3]Department of Statistics and Probability, Michigan State University, East Lansing, Michigan, USA.
[4]Department of Mathematics, University of Siegen, Siegen, Germany.

0043-1397/08/2008WR006858$09.00

[3] Using numerical simulations of fluid flow and solute transport, *Reeves et al.* [2008] used a novel fracture continuum method to produce ensemble particle plumes for a wide variety of random fracture networks. These two-dimensional (2-D) networks are generated according to statistics that describe fracture length, transmissivity, density and orientation. In this paper, we fit the leading edge of ensemble particle plumes to operator-stable densities in order to assess the applicability of a multiscaling fractional-order equation for solute transport predictions in fractured media. Model parameters describing ensemble plume growth rates and primary directions are related to fracture network statistics. An extensive array of fracture network types is analyzed to identify influences of fracture length, transmissivity, orientation, density and presence of multiple fracture groups on transport behavior of a conservative solute.

2. Particle Jumps and Operator-Stable Densities

[4] The multiscaling fractional ADE (MFADE) for solute migration is based on a random walk model:

$$\vec{X} = R^{\mathbf{H}} \cdot \vec{\Theta}, \tag{1}$$

where a random particle jump size vector $\vec{X}$ is the product of two independent random elements: a random growth and scaling matrix $R^{\mathbf{H}}$ and a random direction vector $\vec{\Theta}$ [*Schumer et al.*, 2003a]. The distribution of the scalar R, where $P(R > r) \propto r^{-1}$, is heavy-tailed [*Schumer et al.*, 2003a]. The matrix $\mathbf{H}$ rescales the distribution of jump lengths to account for larger jumps in certain directions:

$$\mathbf{H} = \mathbf{S}\mathbf{H}_o\mathbf{S}^{-1}, \tag{2}$$

where $\mathbf{S}$ and $\mathbf{H}_o$ are, respectively, the eigenvector and eigenvalue matrices for $\mathbf{H}$ [*Schumer et al.*, 2003a]. We address plume growth in two dimensions, which requires only two eigenvectors to represent dominant particle motion directions and two eigenvalues to describe jump magnitudes (and describe plume growth rates) in all directions. Eigenvector and eigenvalue matrices have the form $\mathbf{S} = \begin{bmatrix} e_{11} & e_{21} \\ e_{12} & e_{22} \end{bmatrix}$ and $\mathbf{H}_o = \begin{bmatrix} 1/\alpha_1 & 0 \\ 0 & 1/\alpha_2 \end{bmatrix}$, where column eigenvectors $\vec{e_1}$ and $\vec{e_2}$ are defined in terms of their vector coordinates, and their eigenvalues ($1/\alpha_i$) assign rates of scaling along these directions. The probability decay of particle jump magnitude along the ith eigenvector, R_i, follows a power law: $P(R_i > r) \approx r^{-\alpha_i}$. Particle motion in noneigenvector directions scale according to a mixture of scaling coefficients [*Schumer et al.*, 2003a].

[5] The directional vector $\vec{\Theta}$ in (1) has a distribution around the 2-D unit circle for two-dimensional particle jumps. If particle motion were in three dimensions, $\vec{\Theta}$ would be distributed around the unit sphere. The distribution of directional unit vectors, $M(d\vec{\Theta})$, is called the mixing measure [*Meerschaert et al.*, 2001; *Schumer et al.*, 2003a]. $M(d\vec{\Theta})$ contains the weights or relative intensities of directional particle movement such that $\int_0^{2\pi} M(d\vec{\Theta}) = 1$ [*Meerschaert et al.*, 1999]. In one dimension, mixing measure weights describe the skewness of an α-stable distribution [*Benson*, 1998]. Although mixing measure weights can be either isotropic or anisotropic, it is assumed that the distribution of directional particle movement is anisotropic for solute transport in groundwater flow systems because of the influence of a regional hydraulic gradient [*Schumer et al.*, 2003a].

[6] The particle jumps $\vec{X}$ described by (1) are in an operator-stable domain of attraction [*Meerschaert and Scheffler*, 2001]. The normalized sum of these particle jumps converge in the limit to an operator-stable random vector [*Meerschaert and Scheffler*, 2001]. Operator-stable densities are the most general case of joint α-stable distributions where the rates of scaling ($1/\alpha$) are different along each primary scaling direction. If rates of scaling are equal in all directions, as in the case of a multivariate α-stable distribution, $\mathbf{H}$ reduces to a scalar equal to $1/\alpha$ [*Meerschaert et al.*, 1999]. Multi-Gaussian densities, a subset of operator-stable densities, result when $\mathbf{H_o}$ = *diag*(1/2, 1/2) for two-dimensional plume growth. Multi-Gaussian densities are characterized by elliptical plume geometry with orthogonal, Fickian scaling rates proportional to $t^{1/2}$ along eigenvectors corresponding to the major and minor axes of an ellipse.

[7] Closed-form analytical solutions do not exist for most operator-stable densities. The log-characteristic function of a centered non-Gaussian operator-stable density, (i.e., the logarithm of the Fourier transform of the density), can be represented by *Meerschaert and Scheffler* [2003]:

$$\psi\left(\vec{k}\right) = B\int_0^{2\pi}\int_0^{\infty}\left(e^{i\vec{k}\cdot r^{\mathbf{H}}}\vec{\Theta} - 1 - \frac{i\vec{k}\cdot r^{\mathbf{H}}\vec{\Theta}}{1 + \| r^{\mathbf{H}}\vec{\Theta}\|^2}\right)\frac{dr}{r^2}M\left(d\vec{\Theta}\right), \tag{3}$$

where $B > 0$ provides scale to the density and $\vec{k} \cdot r^{\mathbf{H}\vec{\Theta}} = k_1 r^{1/\alpha_1}\cos(\theta) + k_2 r^{1/\alpha_2}\sin(\theta)$ if $\mathbf{H}$ is diagonal. The inner integral describes the direction and scaling of probability mass for an operator-stable density according to $\mathbf{H}$, while the outer integral distributes probability mass according to weights of the mixing measure, $M(d\vec{\Theta})$. The density, $f(\vec{x})$ of this operator-stable random vector $\vec{X}$ can be computed by taking the inverse Fourier transform [*Meerschaert and Scheffler*, 2003]:

$$f(\vec{x}) = (2\pi)^{-2}\int_{\vec{k}\in\mathbb{R}^2} e^{-i\vec{k}\cdot\vec{x}} e^{\psi\left(\vec{k}\right)} d\vec{k}. \tag{4}$$

The fast Fourier transform [*Strang*, 1988] can also be used to calculate (4).

[8] A multiscaling fractional advection-dispersion equation (MFADE) models solute transport according to operator-stable densities [*Meerschaert et al.*, 2001; *Schumer et al.*, 2003a]:

$$\frac{\partial C(\vec{x}, t)}{\partial t} = -\vec{v}\cdot\nabla C(\vec{x}, t) + \mathcal{D}\cdot\nabla_M^{\mathbf{H}^{-1}} C(\vec{x}, t), \tag{5}$$

where solute concentration, $C(\vec{x}, t)$ changes due to a combination of advective, $\vec{v} \cdot \nabla C(\vec{x}, t)$ and super-Fickian dispersive, $\mathcal{D} \cdot \nabla_M^{\mathbf{H}^{-1}} C(\vec{x}, t)$ effects. The multiscaling fractional derivative, $\nabla_M^{\mathbf{H}^{-1}}$, is parameterized via the scaling matrix $\mathbf{H}$ and mixing measure M (same as $M(d\vec{\Theta})$) to describe directional particle movement. $\mathbf{H}$ is equal in (1), (3) and (5). Values of α_i in $\mathbf{H}$ code one-dimensional spatial fractional-order derivatives where $0 < \alpha_i \leq 2$. Note that [*Meerschaert et al.*, 2001]:

$$\mathcal{F}\left[\nabla_M^{\mathbf{H}^{-1}} C\right]\left(\vec{k}\right) = \psi\left(\vec{k}\right)\hat{C}\left(\vec{k}\right); \tag{6}$$

Table 1. Network Values for Parameter Sets

Set	T[a]	a_1[b]	Density$_1$[c]	θ_1[d], deg	a_2	Density$_2$	θ_2, deg
1	TP	1.0	max/0.0075	30	1.0	max/0.0075	−60
2	TP	1.0	max/0.0018	30	1.0	max/0.0018	−60
3	TP	1.3	int/0.0065	15	1.0	int/0.0065	−30
4	LN	1.3	int/0.0065	15	1.0	int/0.0065	−30
5	TP	1.0	min/0.0080	45	1.6	max/0.0090	−45
6	TP	1.3	max/0.022	60	1.9	max/0.14	−10
7	TP	1.6	max/0.06	30	2.2	int/0.16	−30
8	LN	1.6	max/0.06	30	2.2	int/0.16	−30
9	TP	1.9	int/0.10	45	1.9	int/0.10	−45
10	TP	1.9	min/0.06	45	1.9	max/0.14	−45
11	TP	1.9	max/0.14	45	2.2	max/0.21	−45
12	TP	1.9	int/0.10	45	2.5	max/0.23	−30
13	TP	2.5	min/0.12	45	2.8	min/0.15	−45
14	TP	2.5	max/0.23	45	2.8	max/0.25	−45
15	LN	2.5	max/0.23	45	2.8	max/0.25	−45
16	TP	2.8	min/0.15	45	3.0	min/0.15	−45
17	TP	2.8	int/0.20	45	3.0	int/0.20	−45
18	TP	3.0	max/0.25	30	2.8	max/0.25	10
19	LN	3.0	max/0.25	30	2.8	max/0.25	10

[a]Transmissivity distribution where TP and LN denote truncated Pareto and lognormal, respectively.
[b]Fracture length power law exponent value.
[c]Spatial fracture density [m/m^2].
[d]Fracture set orientation from horizontal in degrees.

that is, a multiscaling fractional derivative is equivalent to multiplying by the log characteristic function of an operator-stable density (3) in Fourier space. Linear advective velocity, $\vec{v}$ in (5) provides a vector shift to the operator-stable density, while a constant dispersion coefficient, $\mathcal{D}$, provides scale to the mixing measure. Note that B in (3) and $\mathcal{D}$ in (5) are proportional.

[9] The goal of this study is to investigate the applicability of the multiscaling fractional-order ADE (MFADE) as a suitable model for ensemble plumes in a fractured medium. Point source solutions to the MFADE are operator-stable probability densities. Hence, we fit ensemble plume data to the operator-stable model by estimating the parameters $\mathbf{H}$ (the scaling matrix) and $M(d\vec{\Theta})$ (the mixing measure) for each set of realizations. After carefully assessing the quality of fit, we then proceed to study the relationship, if any, between the MFADE parameters and the statistical properties of the fracture networks.

3. Results and Discussion

[10] For each of 23 parameter sets, particle plumes from 500 realizations are assessed to determine whether their relative concentration can be adequately fit by either operator-stable or multi-Gaussian density functions. The relative concentration of particle displacements is computed from the difference between final and initial particle locations at a given time increment (deconvolution), so that the resulting plume should correspond to the Green's function solution of the transport equation. The first 19 parameter sets (Table 1) consist of simple networks comprising only two fracture groups with constant orientation. The remaining 4 parameter sets are used to investigate more complex networks where fracture orientation is allowed to deviate around a mean orientation and/or more than two fracture groups are present. Relationships between fracture network statistics such as fracture length, density, transmissivity, variable fracture group orientation and the influence of multiple fracture groups and resultant particle transport are identified.

3.1. Analysis of Ensemble Particle Displacement Plumes

[11] Ensemble particle plume snapshots (e.g., Figure 1) represent a 2-D joint density and consist of all particle displacements over a given time interval of a single parameter set (Table 1). Fitting ensemble particle displacement vectors to operator-stable densities is facilitated by analysis of the marginal distributions of particle displacement. By definition, if ensemble particle clouds can be approximated by an operator-stable density, then marginal distributions of particle displacement should fit α-stable densities [*Meerschaert and Scheffler*, 2001]. If particle clouds resemble a multi-Gaussian density, then marginals will fit a normal density.

[12] To evaluate the marginal distributions of joint ensemble particle plumes, the coordinate directions (eigenvectors) that dominate plume growth must be identified; otherwise the variation in tail behavior will be masked by the plume growth direction with the heaviest tail [*Meerschaert and Scheffler*, 2003]. *Meerschaert and Scheffler* [2003] propose the use of a sample covariance matrix to estimate the eigenvectors of an operator-stable scaling matrix. However, the computation of eigenvectors from a sample covariance matrix leads to eigenvectors with orthogonal orientations. Orientations of fracture groups are not always orthogonal [e.g., *Munier*, 2004], and our simulations demonstrate that nonorthogonal fracture group orientations can lead to nonorthogonal directions of plume growth. In the absence of a rigorous method to identify dominant plume growth directions, eigenvector directions are identified by visual analysis of ensemble particle displacement plumes. A transformation to the coordinates defined by these eigenvectors (denoted as column vector components, e_{ij}) maps particle displacement vectors, $\vec{X}$, from Cartesian coordinates (X_1, X_2) onto a

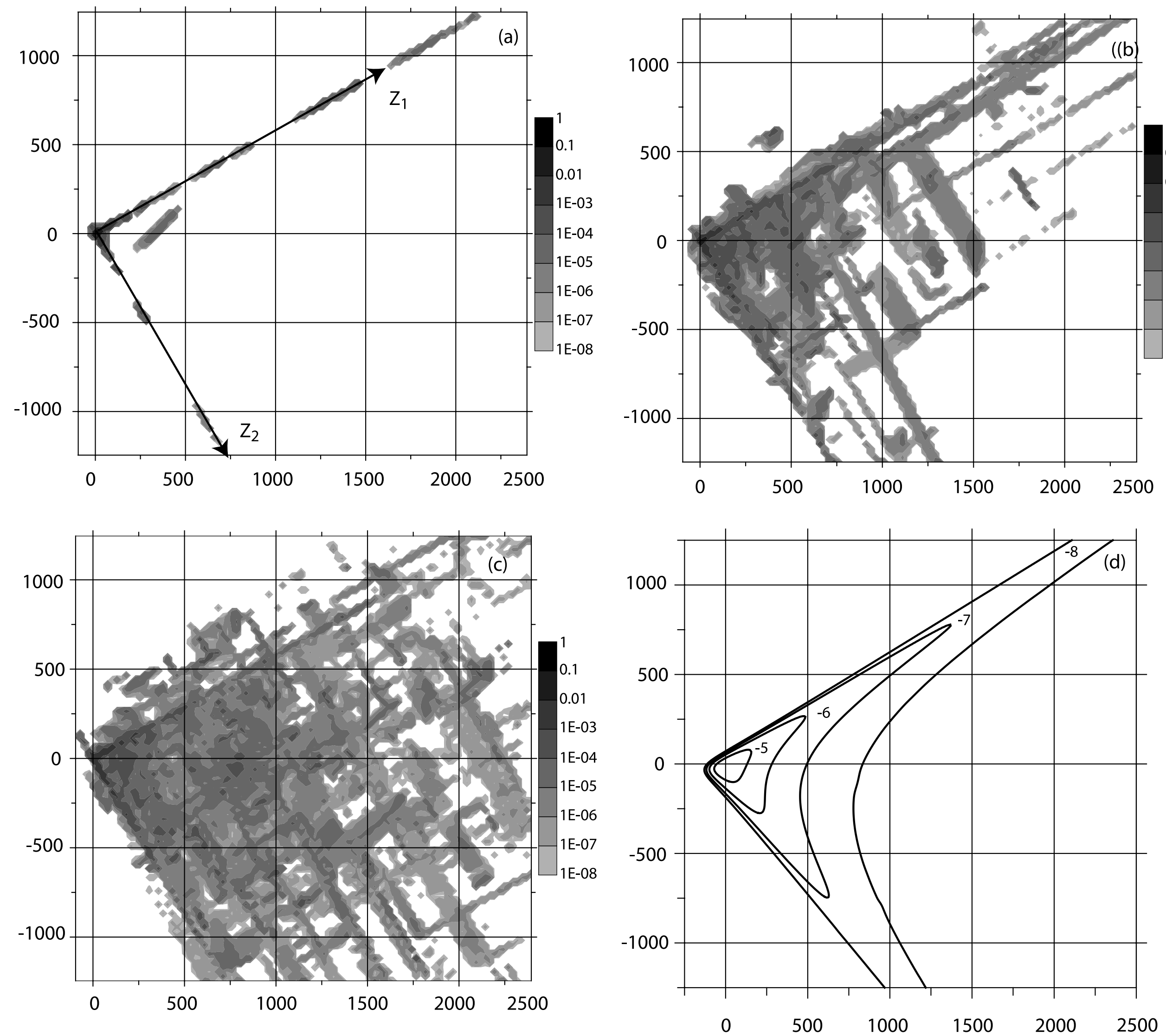

Figure 1. Ensemble particle displacement plumes for set 1 at transport times of (a) 4.6, (b) 10, and (c) 464 years along with (d) an operator-stable density based on the characterization of the ensemble particle displacement plume shown in Figure 1a. For very sparse networks, fast particle transport is dependent on the presence of long continuous fractures with high transmissivity values. The operator-stable plume in Figure 1d closely resembles the ensemble plume in Figure 1a. It is anticipated that ensemble plumes generated from a much greater number of realizations will more closely resemble the shape of the operator-stable density. All spatial values are given in units of meters.

new coordinate system (Z_1, Z_2) [*Meerschaert and Scheffler*, 2003]:

$$\begin{bmatrix} Z_1 \\ Z_2 \end{bmatrix} = \begin{bmatrix} X_1 \\ X_2 \end{bmatrix} \begin{bmatrix} e_{11} & e_{21} \\ e_{12} & e_{22} \end{bmatrix}^{-1}. \tag{7}$$

The resulting marginals Z_1 and Z_2 can then be analyzed for power law content. Coordinates were selected on the basis of plume type. For plumes resembling operator-stable densities, Z_1 and Z_2 represent projections along eigenvectors that are the most and least positive in orientation relative to the hydraulic gradient (e.g., Figure 1a), while Z_1 and Z_2 represent particle motion along major and minor plumes axes, respectively, for multi-Gaussian plumes (e.g., Figure 2).

3.1.1. Estimation of Scaling Matrix, H

[13] An upper truncated Pareto (power law) model is used to estimate tail thickness of the r largest marginal particle jumps for super-Fickian plumes [*Aban et al.*, 2006]:

$$P(Z > z) = \frac{\gamma^{\alpha}(z^{-\alpha} - \nu^{-\alpha})}{1 - \left(\frac{\gamma}{\nu}\right)^{\alpha}}, \tag{8}$$

where Z are marginal particle displacements (Z_1 or Z_2), γ and ν are the minimum and maximum values of Z and α describes the power law tail of the distribution. The use of a truncated Pareto, which has finite moments of all orders, appears to contradict the use of heavy-tailed (infinite variance) statistics required by (5). However, the truncation of the power law trend observed in the distribution of

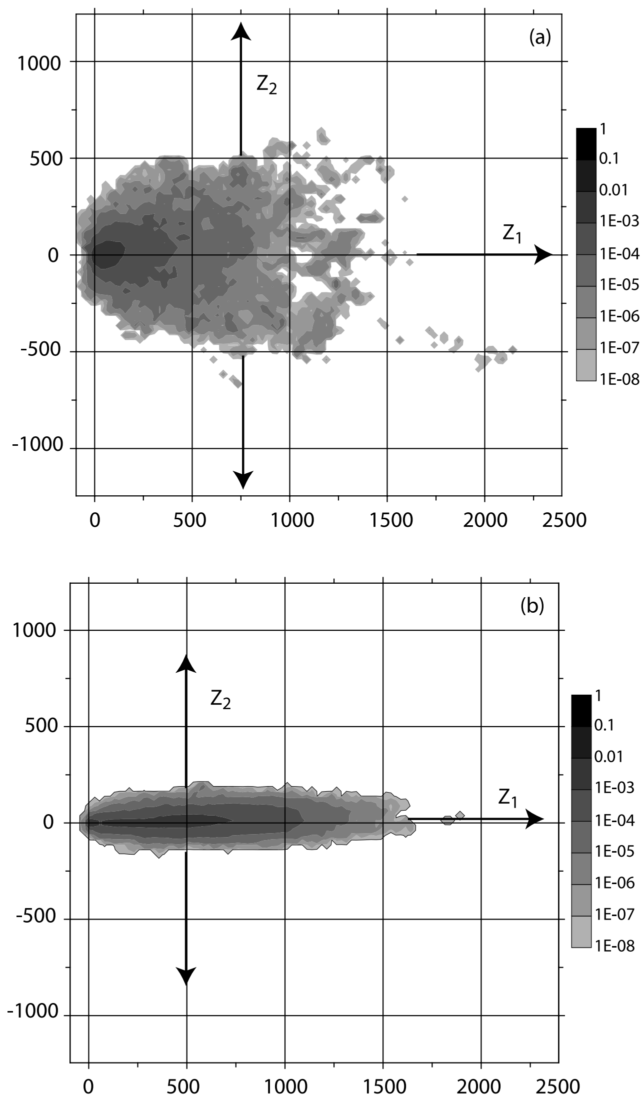

Figure 2. Ensemble particle displacement plume for (a) set 16 and (b) set 17 at transport times of 44,640 and 1000 years, respectively. The only difference between the fractured domains is that set 16 (Figure 2a) has a lower density than set 17 (Figure 2b). The decrease in density from set 17 to set 16 decreases in fluid flux through the network and enhances transverse plume spreading as particles tend to follow fracture orientations (±45°). Both of these factors decrease plume migration rates. In fracture networks with short fracture lengths, fracture pathways become truncated at higher fracture densities (i.e., set 17 (Figure 2b)), and a fracture medium begins to approach an equivalent porous medium. All spatial values are given in units of meters.

marginal particle displacements naturally arises from a finite sampling of heavy-tailed distributions of fracture lengths within a finite model domain. Since particle transport occurs exclusively within a subset of fractures of a network called the hydraulic backbone, solute particles only experience a small subset of fracture lengths and velocities. This is particularly true for the sparsely to moderately connected fracture networks with long fracture lengths that promote the formation of operator-stable densities. Additional limitations on maximum particle distance are imposed by the distribution of fracture transmissivity and lack of within-fracture dispersion which leads to "piston flow" along dominant transport fractures [*Reeves et al.*, 2008].

[14] A maximum likelihood estimation (MLE) estimator [*Aban et al.*, 2006] was coded and used to solve for the truncated Pareto estimated parameters $\hat{\gamma}$ and $\hat{\alpha}$ for each of the marginal distributions:

$$\frac{r}{\hat{\alpha}} + \frac{r\left(\frac{Z_{(r+1)}}{Z_{(1)}}\right)^{\hat{\alpha}} \ln\left(\frac{Z_{(r+1)}}{Z_{(1)}}\right)}{1-\left(\frac{Z_{(r+1)}}{Z_{(1)}}\right)^{\hat{\alpha}}} - \sum_{i=1}^{r}\left[\ln X_{(i)} - \ln X_{(r+1)}\right] = 0, \qquad (9)$$

where $Z_{(1)}, Z_{(2)}, \ldots, Z_{(n)}$ are ranked in descending order, $\hat{\nu} = Z_{(1)}$ is the largest observed data value and

$$\hat{\gamma} = r^{\frac{1}{\hat{\alpha}}}\left(Z_{(r+1)}\right)\left[n-(n-r)\left(\frac{Z_{(r+1)}}{Z_{(1)}}\right)^{\hat{\alpha}}\right]^{\frac{1}{\hat{\alpha}}}. \qquad (10)$$

[15] On the basis of (9) and (10), estimated values for $\hat{\alpha}$ and $\hat{\gamma}$ were found to be sensitive to the selection of the number r of the largest tail data. To address this problem, $\hat{\alpha}$ and $\hat{\gamma}$ were computed using different values of r between 5% to 25% of the largest particle displacements. Within this range, the standard deviation of $\hat{\alpha}$ was found to vary between 0.14 and 0.25 for our simulations. The chi-square test was used to determine best fit estimated parameters for the upper tail of particle displacements [*Carr*, 2002] (Table 2). Mandelbrot plots are used to verify tail thickness estimates of all power law trends (e.g., Figure 3). Mandelbrot plots are also used to distinguish between exponential ($P(Z > z) \sim \exp(-z)$) and Gaussian ($P(Z > z) \sim \exp(-z^2)$) leading-edge tails (Table 2). For a Mandelbrot plot with log-log coordinates, power law tails for the largest marginal particle displacements have linear trends, while exponential trends are nonlinear and the decay of the largest particle displacements is rapid (i.e., thin tailed).

[16] Values of α corresponding to the spreading rates along primary plume growth directions can be estimated using [*Benson et al.*, 2000; *Schumer et al.*, 2003a]:

$$\sigma = (2Dt)^{1/\alpha}, \qquad (11)$$

where σ is an empirical measure of plume size, based on either standard deviation of particle jump magnitude or the linear distance between quantile pairs (see below), and D is a constant dispersion coefficient. Plume spreading rates for a Fickian growth process ($\alpha = 2$) are proportional to $t^{1/2}$ where σ is equal to the square root of the particle displacement variance and D is a constant Gaussian dispersion coefficient. A super-Fickian growth process, where $0 < \alpha < 2$, has an undefined variance of particle displacement (σ remains a measure of plume size in this case) and has spreading rates proportional to $t^{1/\alpha}$. For an operator-stable process following (5), estimates of α from tail (8) and plume spreading rates (11) should be equal.

[17] Several metrics are used to compute plume size, including the standard deviation of particle jump magnitude, $Q_{(stdev)}$, and quantile pairs $Q_{(0.16,0.84)}$, $Q_{(0.05,0.95)}$ and $Q_{(0.01,0.99)}$ where the subscript refers to fraction of particles behind and ahead. The linear distance between each quantile pair (σ) is plotted against time in log-log coordinates (Figure 4). A linear trend on this plot will have a

Table 2. Tail Characteristics of Parameter Sets

Set	Z_1 Trend[a]	α_1[b]	Z_2 Trend	α_2
1	pl	0.4–0.8	pl	0.9–1.1
2	pl	1.0–1.2	pl	1.3–1.4
3	pl	0.4–0.8	pl	0.4–0.8
4	pl	0.4–0.8	pl	0.4–0.9
5	pl	0.5–0.8	pl	0.5–0.8
6	pl	1.0–1.1	pl	1.3–1.9
7	pl	1.2–1.6	pl/exp($-z$)	1.8–1.9
8	pl	0.8–1.0	pl	1.0–1.2
9	pl	1.7–1.9	pl	1.7–1.9
10	exp($-z$)	NA[c]	exp($-z$)	NA
11	pl/exp($-z$)	1.8–1.9	pl/exp($-z$)	1.8–1.9
12	pl	1.8–1.9	exp($-z$)	NA
13	exp($-z$)	NA	exp($-z$)	NA
14	exp($-z^2$)	NA	exp($-z^2$)	NA
15	exp($-z^2$)	NA	exp($-z^2$)	NA
16	exp($-z$)	NA	exp($-z$)	NA
17	exp($-z^2$)	NA	exp($-z^2$)	NA
18	exp($-z^2$)	NA	exp($-z^2$)	NA
19	exp($-z$)	NA	exp($-z^2$)	NA

[a]Decay trend of largest particle jumps where pl, exp($-z$), and exp($-z^2$) denote power law, exponential and Gaussian, respectively.
[b]Slope of power law decay of largest particle jumps.
[c]NA means not applicable.

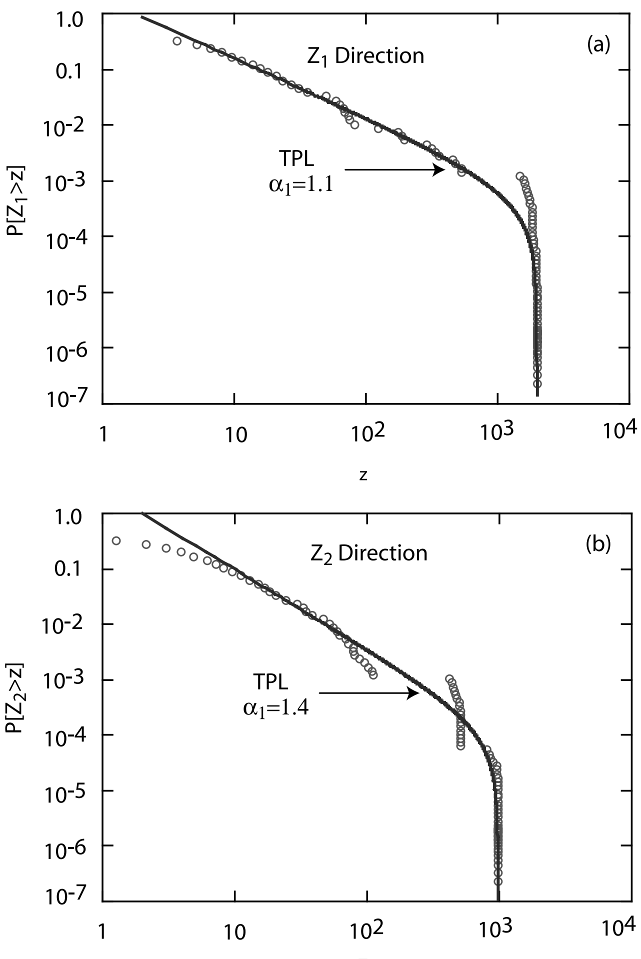

Figure 3. Mandelbrot plots of largest ranked particle displacements (circles) for set 2 along (a) Z_1 and (b) Z_2 with best fit truncated power law (TPL) model at an elapsed time of 0.1 years. Approximately every 1/1000 point is plotted. Values of Z are given in units of meters.

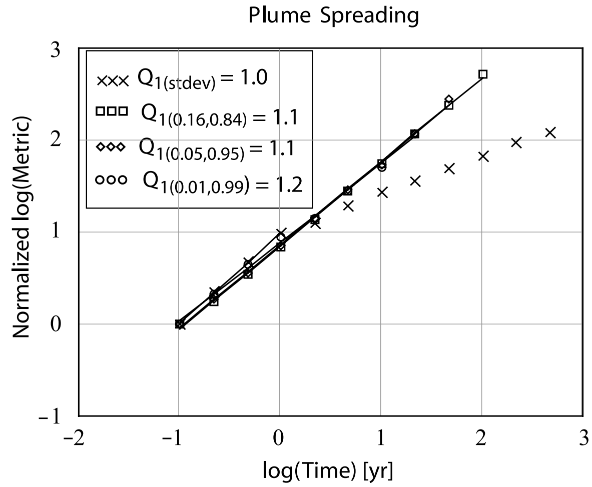

Figure 4. Values of α_1 based on scaling of plume growth along Z_1 for parameter set 2 using all four normalized metrics. Slope of the regression lines is $1/\alpha$. Particles leaving domain boundaries result in undefined quantile estimates for later time steps. Estimates of α based on $Q_{(stdev)}$ are very sensitive to the loss of extreme values. The change of slope in $Q_{(stdev)}$ is caused by a significant loss of particles after the fourth time step.

slope of $1/\alpha$ according to (11). Values of α for sets 1–19 are provided in Table 3. For some parameter sets, quantiles cannot be determined at later time steps because too many particles have left the model domain (a censoring problem).

[18] Eigenvectors and eigenvalues of the scaling matrix **H** in (5) code anistropic plume evolution over time as a super-Fickian growth process. Eigenvectors, $\vec{e_i}$, denote primary plume growth directions and are computed visually from ensemble particle displacement plumes. Primary plume growth directions are presented in degrees from horizontal where $\vec{e_i} = [\cos(\theta_i)\ \sin(\theta_i)]^T$ (Table 4). Eigenvalues ($1/\alpha_i$) describe plume growth rates and are computed from marginal distributions along $\vec{e_i}$. Because of the inverse relationship between α and rates of plume spreading ($1/\alpha$), lower values of α indicate more rapid rates of plume growth. Estimates of α_i obtained from tail and plume spreading rate methods are both used in the determination of eigenvalues, though, in general, values of α for operator-stable plumes most closely reflect the fracture length exponent (Table 4). The influence of fracture length and other network parameters on values of α will be discussed shortly.

3.1.2. Mixing Measure Weights

[19] When all $\alpha_i < 2$, the variance and covariance of particle jumps are undefined. Instead, weights and directions of the mixing measure, $M(d\vec{\Theta})$, describe the dependence structure between eigenvectors of plume growth ($\vec{e_1}$, $\vec{e_2}$) and heavy-tailed particle jumps, $\vec{X}$ [*Meerschaert and Scheffler*, 2001]. This dependence structure codes the relative likelihood of large particle motions in any direction. For fracture networks, mixing measure weights are influenced by the mean ensemble fluid flux through each fracture set, and mixing measure weights are concentrated around mean fracture group orientations. In this study, two methods are used to estimate $M(d\vec{\Theta})$. The first method calculates $M(d\vec{\Theta})$ a posteriori from ensemble particle displacement plumes,

Table 3. Plume Scaling Rates

Set	Z_1				Z_2			
	$Q_{(stdev)}$	$Q_{(0.16,0.84)}$	$Q_{(0.05,0.95)}$	$Q_{(0.01,0.99)}$	$Q_{(stdev)}$	$Q_{(0.16,0.84)}$	$Q_{(0.05,0.95)}$	$Q_{(0.01,0.99)}$
1	1.0	1.1	1.1	1.2	1.1	1.1	1.0	1.1
2	1.0	1.1	1.1	1.2	1.0	1.1	1.1	1.2
3	1.1	1.1	1.1	1.2	1.1	1.1	1.0	1.1
4	1.0	1.1	1.2	1.1	1.1	1.1	1.0	1.3
5	1.1	1.0	1.0	1.0	1.2	1.2	1.1	1.0
6	1.8	1.3	1.4	1.4	1.4	1.2	1.3	2.2
7	1.5	1.5	1.5	2.0	1.2	1.3	1.4	1.8
8	1.5	NA[a]	2.0	1.7	1.2	NA[a]	1.6	1.8
9	1.4	1.4	1.5	1.8	1.3	1.4	1.5	2.0
10	1.5	1.4	1.5	1.9	1.5	1.3	1.5	1.9
11	1.6	1.4	1.5	1.9	1.6	1.4	1.5	1.9
12	1.6	1.4	1.6	2.1	1.6	1.4	1.6	2.3
13	1.6	1.6	1.7	2.2	1.7	1.8	1.9	2.1
14	1.3	1.4	1.4	1.6	2.3	3.1	3.4	2.2
15	1.6	1.6	1.7	2.3	1.6	1.7	1.8	2.1
16	1.6	1.6	1.7	2.3	1.9	1.9	2.0	2.2
17	1.3	1.5	1.5	1.6	2.6	3.1	3.8	3.3
18	1.5	1.4	1.5	1.9	1.3	2.4	2.6	2.8
19	1.3	1.1	1.2	1.6	1.1	1.6	1.9	2.1

[a]Nonlinear trend in log-log space.

while the second method estimates $M(d\vec{\Theta})$ a priori on the basis of a simple computation of mean ensemble fluid flux for each fracture group of a network.

3.1.2.1. A Posteriori Mixing Measure Estimation

[20] A heavy-tailed random vector in the generalized domain of attraction of some operator-stable law, $\vec{Y}$, has the relationship [*Scheffler*, 1999]

$$\vec{Y} = \tau(\vec{Y})^{\mathbf{H}}\vec{\Theta}(\vec{Y}), \tag{12}$$

which describes the dependence structure for directional particle transport, $\vec{\Theta}(\vec{Y}) \in \mathcal{S}$, according to some radius, $\tau(\vec{Y}) > 0$. Values of $\vec{\Theta}(\vec{Y})$ are defined as the position where a rescaled particle jump vector, $\vec{Y}$, with scaling matrix, $\mathbf{H} = \begin{bmatrix} 1/\alpha_1 & 0 \\ 0 & 1/\alpha_2 \end{bmatrix}$, intersects the unit circle of a Jurek coordinate system (Figure 5) [*Jurek*, 1984]. A Jurek coordinate system is an anisotropic polar coordinate system where coordinate axes are scaled according to power law coefficients where $\alpha_1 \neq \alpha_2$ and $\theta_1^2 + \theta_2^2 = 1$. Because of unequal scaling rates, $\tau(\vec{Y})$ is curved. If $\alpha_1 = \alpha_2$, scaling is isotropic and a Jurek coordinate system reduces to a symmetric polar plot.

Table 4. Characterization of **H**

Set	$\vec{e_1}$, deg	α_1	$\vec{e_2}$, deg	α_2
1	30	1.0–1.2	−60	1.0–1.1
2	30	1.0–1.2	−60	1.0–1.2
3	15	1.1–1.2	−30	1.0–1.2
4	15	1.0–1.2	−30	1.0–1.3
5	45	1.0–1.1	−45	1.0–1.2
6	60	1.3–1.4	−10	1.2–1.4
7	30	1.5–1.7	−30	1.8–1.9
8	30	1.5–1.7	−30	1.8–1.9
9	45	1.7–1.9	−45	1.7–1.9
10	45	1.8–1.9	−45	1.8–1.9
11	45	1.8–1.9	−45	1.8–1.9
12	0	1.7–1.9	±90	2.0

[21] Since primary plume growth directions are not necessarily aligned with axes of a Cartesian coordinate system for our simulations, it is advantageous to correct for this before applying (12). By applying the change of coordinates, $\vec{Z} = \mathbf{S}^{-1}\vec{Y}$ where $\mathbf{S}$ represents an eigenvector matrix of plume growth, (12) can be expressed as

$$\vec{Z} = \tau(\vec{Z})^{\mathbf{H}}\vec{\Theta}(\vec{Z}). \tag{13}$$

Values of $\tau(\vec{Z})$ are then computed using a method presented by *Meerschaert and Scheffler* [2003] where Pareto distributions, $P(X > x) = wx^{-\alpha}$, are used to appropriately scale $\vec{Z}$ along coordinate axes. Values of α for the Pareto distributions are estimated using (8) (Table 2), while values of w are computed using the relationship $w = \gamma^{\alpha}$ [*Aban et al.*, 2006]. Next, values of $\tau(\vec{Z})$ are ranked in descending order, $\tau(\vec{Z_1})$, $\tau(\vec{Z_2})$,. . .,$\tau(\vec{Z_n})$, where n is based on percentages used in (8)

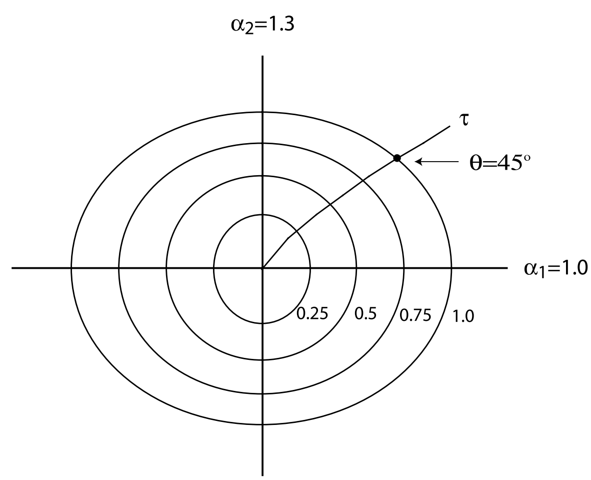

Figure 5. Jurek coordinate system where $\alpha_1 = 1.0$ and $\alpha_2 = 1.3$ lead to unequal directional scaling rates. The value of θ is defined as the position where the curved radius, τ, intersects the unit circle.

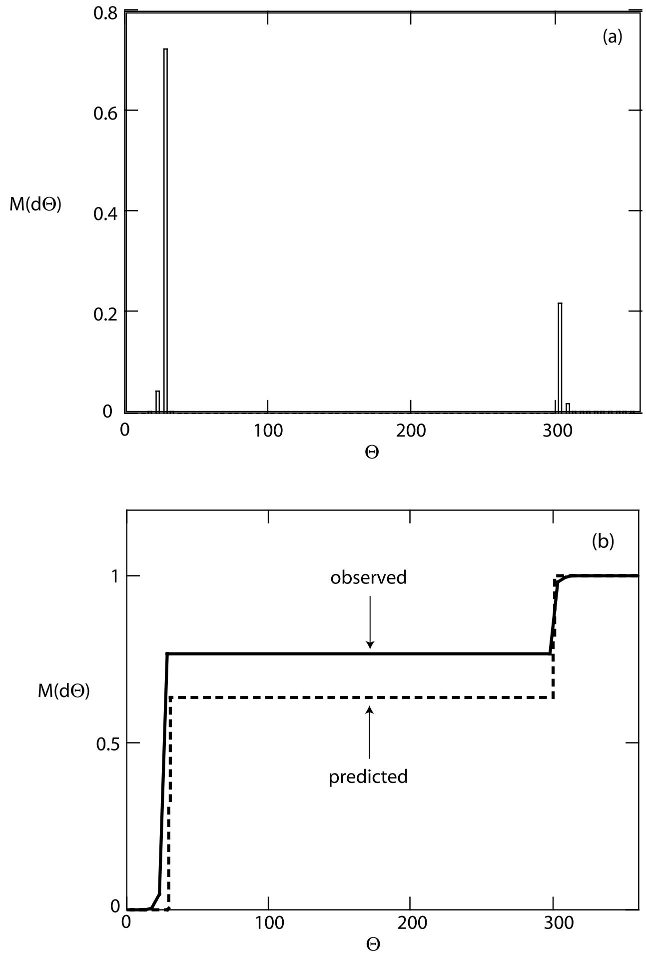

Figure 6. (a) Histogram and (b) cumulative distribution plot of mixing measure weights for set 1 at a transport time of 0.46 years observed from the ensemble particle plume (solid line) and predicted from the ensemble flux calculation (dashed line). Note the concentration of mixing measure weight in the direction of fracture group orientations, 30° and −60°. The difference between the predicted and observed weights is approximately 9%.

for the computation of γ and $\underset{\sim}{\alpha}$. Finally, values of $\Theta(\vec{Z})$, computed from the largest $\tau(\vec{Z})$ values, are transformed back to the original coordinate system using the relationship, $\vec{\Theta}(\vec{Y}) = \mathbf{S}\vec{\Theta}(\vec{Z})$. Values of $\vec{\Theta}(\vec{Y})$ are binned into 5° increments and normalized to provide relative weights for $M(d\vec{\Theta})$ (e.g., Figure 6) [*Scheffler*, 1999].

3.1.2.2. A Priori Mixing Measure Estimation

[22] A simple relationship between fracture group orientation and density may be used to estimate $M(d\vec{\Theta})$ a priori on the basis of an idealized computation of ensemble-averaged fluid flux:

$$q_\theta = \rho_\theta \langle K_\theta \rangle J_\theta, \tag{14}$$

where q_θ, the mean ensemble fluid flux occurring through fractures oriented at θ from a mean hydraulic gradient, is the product of ρ_θ, the ratio of fracture density oriented at θ to the total network fracture density (i.e., the density over all θ), and J_θ, the projected mean gradient onto fractures oriented at θ, where $J_\theta = |||\nabla h|| \cdot \cos(\theta)|$. Transmissivity values assigned to individual fractures are independent of fracture orientation for all simulations [*Reeves et al.*, 2008]. Therefore, in the computation of (14), the ensemble-averaged hydraulic conductivity $\langle K_\theta \rangle$ is considered constant over all θ. Normalized values of q_θ represent $M(d\vec{\Theta})$.

[23] On the basis of (14), networks containing fracture groups with constant orientation will contain nonzero values of $M(d\vec{\Theta})$ only when θ is equal to the orientation of a fracture group, and the orientation of the fracture group is nonorthogonal to the mean hydraulic gradient (e.g., Figure 6). For more complex cases when θ is allowed to deviate around a mean fracture group orientation, a probability distribution (i.e., Fisher or Bingham [*Bingham*, 1964]) can be used to define ρ_θ (e.g., Figure 7).

3.2. Influence of Fracture Length

[24] Trace lengths of natural rock joints and faults are often observed to be distributed according to power law models [e.g., *Bour and Davy*, 1997; *Renshaw*, 1999; *Bonnet et al.*, 2001]. A Pareto probability distribution is used to assign fracture trace lengths in our simulations:

$$P(Y > y) = wy^{-a}, \tag{15}$$

where the power law exponent, a, typically lies between 1 and 3 [e.g., *Bour and Davy*, 1997; *Renshaw*, 1999; *Bonnet et al.*, 2001] and the scalar w is a function of the minimum fracture length (5 m). In general, sample mean fracture length and a are inversely related. For $a < 2$, the variance and standard deviation of fracture length diverge and a characteristic fracture length is undefined. If a strong correlation exists between a and estimates of α on the basis of both plume spreading rates and power law probability decay of largest particle jumps, then a is the only statistic necessary to distinguish between super-Fickian ($a < 2$) and Fickian ($a \geq 2$) transport regimes.

[25] We investigate the influence of fracture length exponent on ensemble particle transport over the range ($1.0 \leq a \leq 3.0$) of power law exponent values (Figure 8). On the basis of network connectivity studies [e.g., *Renshaw*, 1999; *de Dreuzy et al.*, 2001], parameter sets 1–19 are divided into 3 groups on the basis of fracture length exponent values. These groups define domains where network properties are dominated by either long fractures with $1.0 \leq a \leq 1.6$ (sets 1–5), a combination of both short and long fractures $1.9 \leq a \leq 2.2$ (sets 9–11), or short fractures $2.5 \leq a \leq 3.0$ (sets 13–19). Parameter sets 6, 7 and 12 are used to explore overlaps between groups.

3.2.1. Group 1: 1.0 ≤ *a* ≤ 1.6

[26] For low values ($1.0 \leq a \leq 1.6$) of trace length exponents (sets 1–5), connectivity and transport properties are dominated by a few, very long fractures that span a large area of the model domain. The dominance of these fractures is apparent from the ensemble particle plumes that preserve the features of individual transport realizations (Figure 1). Early arrival times of particles at exit boundaries are dependent on both the presence of very long fractures and high fracture transmissivity values. This indicates the presence of strong sample to sample fluctuations for individual realizations [*Follin and Thunvik*, 1994]. The first particles leave the model domain for set 1 (a_1 = 1.0, a_2 = 1.0) at approximately 2 years. In this particular realization, all 25,000 particles leave the northern domain boundary

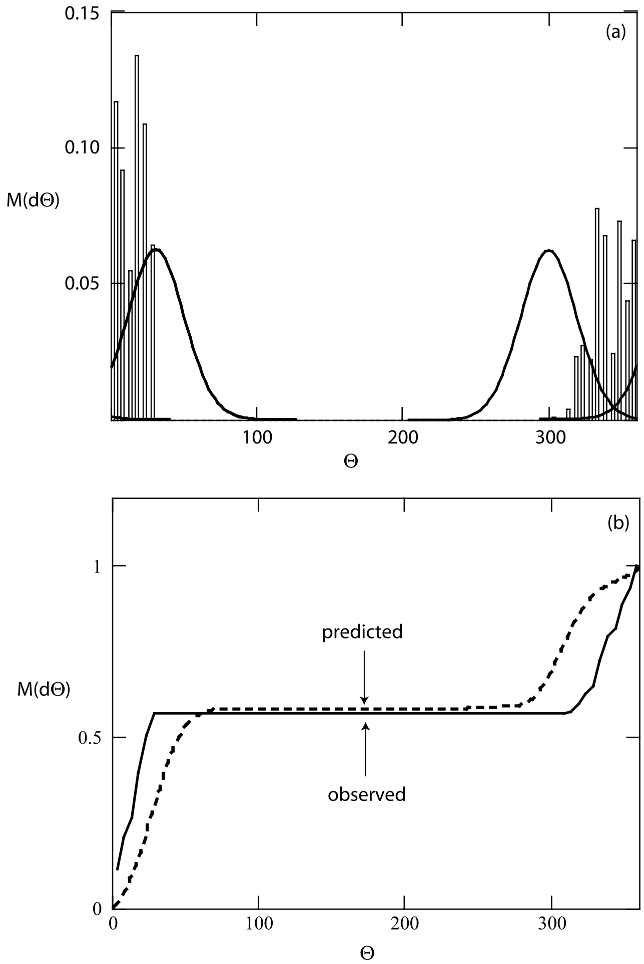

Figure 7. (a) Histogram and (b) cumulative distribution plot of mixing measure weights for set 20 at transport time of 100 years observed from the ensemble particle plume (solid line) and predicted from the ensemble flux calculation (dashed line). Fisher distribution curves are presented in Figure 7a for comparison of mixing measure weights with the distribution of fracture orientation, according to mean group orientations of 30° and −60°. Mixing measure weights are clustered around the mean hydraulic gradient. This is caused by the preferential movement of particles in fractures that are more favorably aligned in the direction of the mean hydraulic gradient. Note that the observed mixing measure weights are more clustered in the direction of the mean hydraulic gradient than predicted by the ensemble flux calculation.

through a single, highly transmissive fracture that spans the entire model domain.

[27] The parameter α describes the power law leading edge of the particle plume. Estimates of α for the leading edges of the set 1 ensemble range between 0.4–0.8 for Z_1 and 0.9–1.1 for Z_2 (Table 2 and Figure 9). Though fracture length exponents a_1 and a_2 are identical, differences in fracture orientation relative to the hydraulic gradient (θ_1 = 30°, $\theta_2 = -60°$) may explain higher values of α along the Z_2 axis. The presence of very heavy leading-edge distribution tails along Z_1 for early time steps are close to the power law exponent value assigned to fracture transmissivity (a_T = 0.4), suggesting that tail estimates of α for networks

a_1/a_2	1.0	1.3	1.6	1.9	2.2	2.5	2.8	3.0
1.0	X							
1.3	X							
1.6	X							
1.9		X		X				
2.2			X	X				
2.5				X				
2.8						X		
3.0							X	

Figure 8. Investigated regions (crosses) into the parameter space for fracture length exponents, a_1 and a_2.

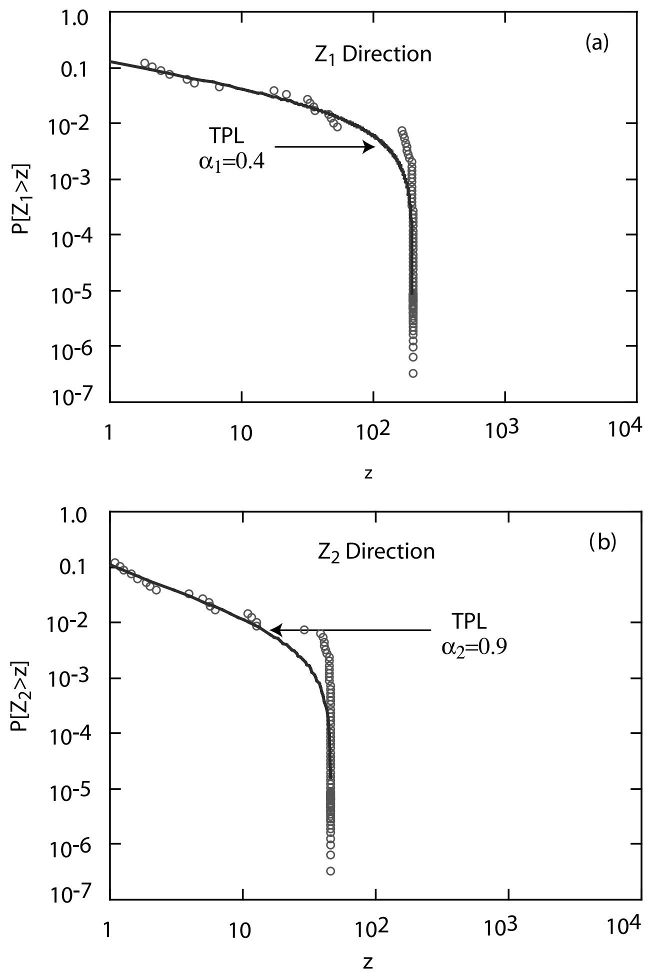

Figure 9. Mandelbrot plots of largest ranked particle displacements (circles) for set 1 along (a) Z_1 and (b) Z_2 with best fit truncated power law (TPL) model at an elapsed time of 0.1 years. Fast transport in very sparse networks is dominated by long, domain-spanning fractures; therefore, the influence of the transmissivity distribution can be observed at very early transport times. Values of α estimated from particle displacements are lower than the fracture length exponents used to generate the network (a_1 = a_2 = 1.0) and to reflect the tail of the transmissivity distribution (a_T = 0.4). Approximately every 1/1000 point is plotted. Values of Z are given in units of meters.

dominated by very long fractures primarily reflect the distribution of fracture transmissivity. Early time tail estimates for set 1 are dependent only on the distribution of fracture transmissivity, since the upper tail of marginal particle displacements consists of realizations where particle transport occurs through only one or a few fractures that span the entire domain. Interaction between these long, dominant fractures and other less significant fractures with shorter lengths and lower transmissivity values are minimal. This is further supported by estimates of α based on plume spreading rates and the distribution of mixing measure weights. Values of α based on plume spreading rates are near 1.0, indicating ballistic transport along long fractures where little or no mixing occurs between flow paths. This is analogous to differential advection in a stratified aquifer [*Mercado*, 1967].

[28] Both observed (measured from ensemble plumes) and predicted (estimated from fluid flux) mixing measure weights are highly concentrated along primary fracture group orientations ($\theta_1 = 30°$, $\theta_2 = -60°$) for all time steps (Figure 6). The difference between observed and predicted mixing measure weights is small (approximately 9%). The observed mixing measure weight may be overestimated for particles traveling along the fracture group oriented at 30°, since these weights are calculated using the greatest 10% of the ensemble particle displacements, and particles traveling along the fracture group oriented at 30° can travel a greater distance before exiting the model domain than those in the fracture group oriented at −60°. Furthermore, particles leaving the model domain cause the observed mixing measure weights to vary over time, suggesting that a priori estimates of mixing measure weights based on fluid flow are more reliable.

[29] The operator-stable density shown in Figure 1 adequately captures the most significant features of ensemble particle displacements for set 1, including: nonelliptical plume geometry, where plume growth directions correspond to fracture group orientations; power law tails of the largest particle displacements; and super-Fickian plume growth rates. Since there are significant differences between individual realizations, these plumes may be considered pre-ergodic. A detailed study of the approach to ergodic conditions is the subject of another paper (D. M. Reeves et al., The influence of fracture statistics on advective transport and implications for geologic repositories, submitted to *Water Resources Research*, 2007).

[30] Parameter sets 3 ($a_1 = 1.3$, $a_2 = 1.0$) and 5 ($a_1 = 1.0$, $a_2 = 1.6$) within this group emphasize the influence of different fracture length exponents on solute transport. The separation distance between fracture length exponents is 0.3 for set 3 and 0.6 for set 5. Tail values of α for Z_1 and Z_2 are similar for both sets and range between 0.4–0.8 for set 3 and 0.5–0.8 for set 5. Again, low tail estimates reflect the influence of a heavy-tailed transmissivity distribution ($a_T =$ 0.4). Relatively equal tail estimates of α along Z_1 and Z_2 indicate that differences in fracture length exponents for fracture networks, where fracture length exponents for both sets are in group 1, do not significantly influence rates of particle transport. Estimates of α based on plume spreading rates (1.0–1.2) for sets 3 and 5 are higher than tail estimates and indicate ballistic transport where minimal flow path mixing occurs. This mismatch between the tail power law and the power law rate of spreading also shows that the operator-stable process does not capture the ensemble plume near the source area. Addressing this shortcoming using a more sophisticated model that also accounts for particle retention is the subject of future work. The measured mixing measure weights for sets 3 and 5 are similar to set 1, where $M(d\vec{\Theta})$ is concentrated along fracture group orientations.

3.2.2. Group 1 and Group 2 Mix

[31] Sets 6 ($a_1 = 1.3$, $a_2 = 1.9$) and 7 ($a_1 = 1.6$, $a_2 = 2.2$) explore the transition between fracture length exponent group 1 ($1.0 \leq a \leq 1.6$) and group 2 ($1.9 \leq a \leq 2.2$). Networks for sets 6 and 7 both contain fracture groups where one fracture group primarily consists of long fractures while the other consists of a combination of short and long fractures. To study contributions of each fracture group on overall particle transport, fracture group orientations ($\theta_1 = 60°$, $\theta_2 = -10°$) for set 6 are intended to minimize the influence of the mean hydraulic gradient along the fracture group with the lower fracture length exponent value ($a_1 = 1.3$), while maximizing the influence of the mean hydraulic gradient along the fracture group with the higher fracture length exponent value ($a_2 = 1.9$). This contrast is not reflected in the leading edges, since estimated values of α along Z_1 and Z_2 range between 1.0–1.1 and 1.3–1.9, respectively. These numbers are more consistent with fracture length exponents. With the exception of $Q_{(0.01,0.99)}$, plume spreading α estimates ($\alpha_1 =$ 1.3–1.4, $\alpha_2 = 1.2$–1.4) are in general agreement with tail values along Z_1 and are generally lower than predicted by the tail for Z_2.

[32] Since the primary metrics used to quantify plume spreading rates are based on the distance between particles representing quantile pairs ($Q_{(0.16,0.84)}$, $Q_{(0.05,0.95)}$, $Q_{(0.01,0.99)}$), lower estimates of α for plume spreading rates than tail estimation methods are most likely caused by particle retention in low-velocity fractures. Retention of particles within the source area increases interquantile distance, which results in lower estimates of α on the basis of growth rate (i.e., the plume appears to grow more rapidly than the leading half of the plume would indicate). The α estimates based on the leading tails are not sensitive to retention, since these particles spend little or no time in slow fractures [see also *Schumer et al.*, 2003b]. Similarly, our estimates of the mixing measure are based on the fastest particles and are not affected by the retention. However, particle retention in low-velocity segments of the hydraulic backbone dictates that increased accuracy of prediction near the source would be achieved by coupling our solutions to either a continuous time random walk (CTRW) model [*Berkowitz and Scher*, 1997; *Scher et al.*, 2002; *Dentz and Berkowitz*, 2003; *Bijeljic and Blunt*, 2006] or a multirate mobile-immobile model [*Haggerty and Gorelick*, 1995; *Haggerty et al.*, 2000; *Schumer et al.*, 2003b; *Baeumer et al.*, 2005]. A detailed study of the long-term particle retention and the validity of the ergodic hypothesis is investigated in another study (Reeves et al., submitted manuscript, 2007).

[33] Set 7 ($a_1 = 1.6$, $a_2 = 2.2$) contains one fracture group with infinite variance lengths and another with finite variance. Estimates of α reflect this contrast as tail estimates for Z_1 range between 1.4 and 1.6, while tails along Z_2 vary

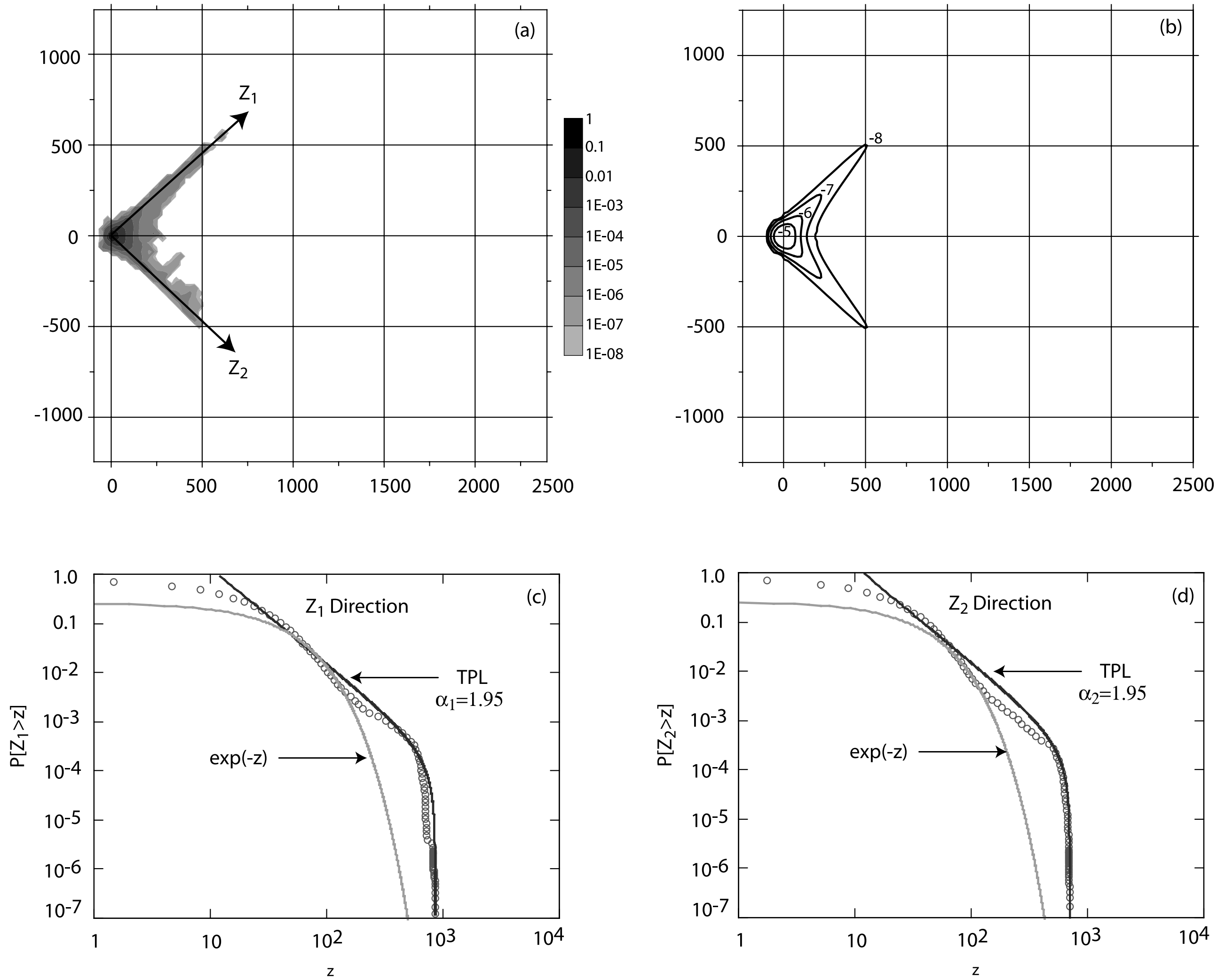

Figure 10. (a) Ensemble particle displacement plume for set 11 at a transport time of 21 years along with (b) best fit operator-stable density and Mandelbrot plots of largest ranked particle displacements (circles) along (c) Z_1 and (d) Z_2 with best fit truncated power law (TPL) and exponential ($\exp(-z)$) models. Networks containing a combination of infinite variance and finite variance distributions of fracture length (a_1 = 1.9, a_2 = 2.2) produce solute plumes with super-Fickian growth rates and leading plume edges that appear to show a transition between power law and exponential decay of the largest particle jumps.

between a very weak power law (1.9) and exponential decay. The marginal jumps in the Z_2 direction did not converge to a Gaussian, but power law content was sharply reduced. Consistent with an operator-stable model, the jumps in the two directions are independent and the finite variance fracture group (Z_2) did not strongly influence particle motion along the infinite variance fracture group (Z_1). With the exception of $Q_{1(0.01,0.99)}$, estimates of α based on plume spreading rates along Z_1 (1.5) are in agreement with tail estimates (1.4–1.6). Lower values of α for plume spreading rates along Z_2 (1.2–1.8) indicate particle retention in fractures with low transmissivity values.

3.2.3. Group 2: $1.9 \leq a \leq 2.2$

[34] Group 2 ($1.9 \leq a \leq 2.2$) represents a transition between the infinite variance of group 1, and the finite variance fracture lengths of group 3, although the lower end of the fracture length exponent range is near the finite variance threshold (2.0). Parameter sets 9 and 11 are used to further investigate the transition between heavy-tailed and exponential to Gaussian transport. Similar to group 1 networks, eigenvectors of plume growth in sets 9 and 11 correspond to fracture group orientations. However, the primary difference between group 1 and group 2 networks is that the leading plume edge may exhibit either a slight power law or exponential tail (Table 2).

[35] Tail estimates (1.8–1.9) for set 9 (a_1 = 1.9, a_2 = 1.9) confirm that particles traveling through networks containing fracture groups with fracture length exponents near the finite variance cutoff (a = 2) can experience heavy-tailed transport. Tails of the largest particle displacements for set 11 (a_1 = 1.9, a_2 = 2.2) appear to show a transition between a weak power law and exponential trend (Figure 10). Though a strong power law trend is not observed in the leading plume edge for set 11, the plume most closely resembles an operator-stable density (Figure 10b) with α values of 1.8. Estimates of α from plume growth rates show large vari-

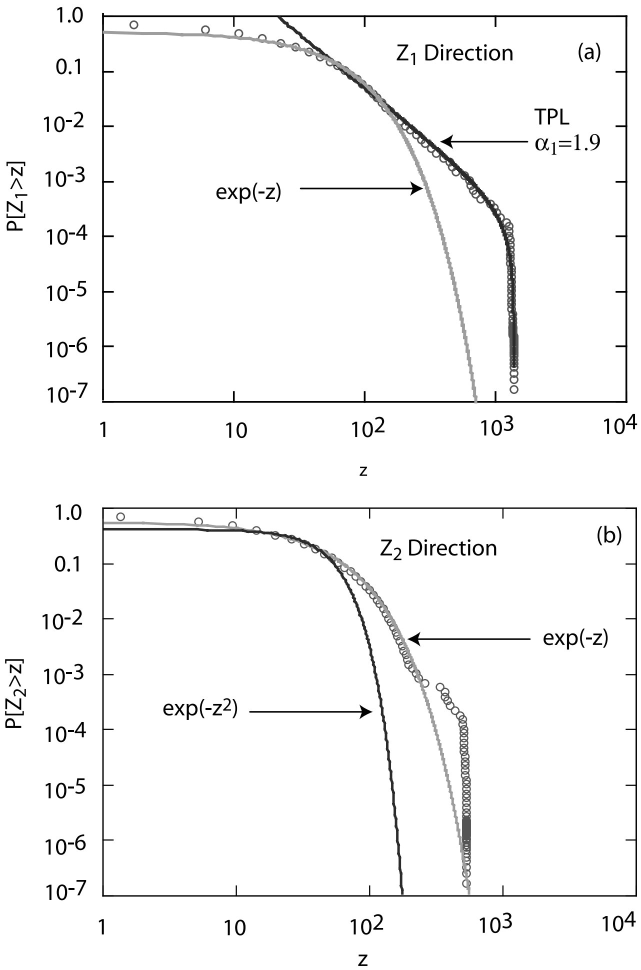

Figure 11. Mandelbrot plots of largest ranked particle displacements (circles) for set 12 along (a) Z_1 with best fit power law (TPL) and exponential ($\exp(-z)$) and (b) Z_2 with best fit exponential ($\exp(-z)$) and Gaussian ($\exp(-z^2)$) at an elapsed time of 1 year. Note that the largest ranked particle displacements show a power law trend along Z_1 (a_1 = 1.9), while an exponential decay is observed along Z_2 (a_2 = 2.5). Approximately every 1/1000 point is plotted. Values of Z are given in units of meters.

ability along the two primary growth directions (1.4–1.9), but are in general agreement with the α value used to generate the operator-stable plume (1.8). This suggests that super-Fickian transport predominantly occurs for group 2 networks.

3.2.4. Group 2 and Group 3 Mix

[36] Only one parameter set, set 12 (a_1 = 1.9, a_2 = 2.5) was designed to investigate networks containing fracture groups with fracture length exponent values in the range of both group 2 and group 3. The level sets of the ensemble particle plume for this parameter set are approximately elliptical (not shown), with a strong power law trend of the decay of largest particle displacements (α = 1.8–1.9) in the longitudinal direction (Z_1) and more exponential tailing in the transverse (Z_2) direction (Figure 11). The different type of tail decay in each direction can be attributed to the difference that exists between fracture length exponents (0.6). The fracture group with shorter fractures (a_2 = 2.5) essentially enhances connectivity between longer fractures of the other set (a_1 = 1.9), allowing transport to occur predominantly along Z_1. Thus, the influence of longer fractures on solute transport is preserved. An ADE with fractional-order derivatives in the longitudinal direction and integer-order derivatives in the transverse direction can describe this motion process [*Schumer et al.*, 2003a].

3.2.5. Group 3: 2.5 $\leq a \leq$ 3.0

[37] Multi-Gaussian transport occurs in networks where fracture length exponents are in group 3 (2.5 $\leq a \leq$ 3.0) (sets 13–19). Differences between Gaussian and operator-stable motion processes are easily observable. First, correlations between fracture group orientations and eigenvectors of plume growth become weak to nonexistent. This leads to orthogonal scaling directions according to the major and minor plume axes (Figure 2). Second, exponential or Gaussian tails are observed for all sets (Table 2). Plume spreading rates ($1/\alpha$) for all sets in group 3 (13–19) suggest that fractures with low transmissivity values act as a retention mechanism, and especially affect rates of solute transport in the longitudinal direction, Z_1 (Table 3). Estimates of $\alpha < 2$ would usually indicate super-Fickian transport; however, in this case, the tendency of particles to remain near the source increases interquantile distances, and consequently rates of scaling [see *Berkowitz and Scher*, 1995, 1997; *Baeumer et al.*, 2005]. Spreading rates in the transverse direction, Z_2, are not as heavily influenced.

[38] The fit between empirical distributions of marginal particle jumps and a theoretical Gaussian varies and is heavily influenced by the retention of particles in short fractures with low transmissivity values, especially for transport in the longitudinal direction (Figures 12 and 13). In addition to particle retention near the source, fracture spatial density was found to determine whether the distribution of marginal particle jumps follow either an exponential or Gaussian trend. This subject will be further discussed in the next section.

3.3. Influence of Spatial Fracture Density

[39] Fracture spatial density, ρ_{2D}, is highly dependent on the distribution of fracture lengths in a model domain [*Renshaw*, 1999] and is defined as the ratio between the sum of individual fracture lengths, l_i and domain area, A:

$$\rho_{2D} = \frac{1}{A}\sum_{i=1}^{n} l_i. \tag{16}$$

For each power law exponent, spatial density values are assigned to represent sparsely (min), moderately (int) and densely (max) fractured domains (Table 1). Values for spatial density range from at, or slightly above, the percolation threshold for the sparely fractured domains to maximum reported density values [*Renshaw*, 1997; *Ehlen*, 2000] for the densely fractured domains. Density values assigned to moderately fractured domains lie directly between values representing sparsely and densely fractured domains. To investigate the influence of spatial density on particle transport, values of fracture length exponents and orientations are kept constant for each set in the following pairs: sets 1–2, 9–10, 13–14, and 16–17. Only values of spatial density are changed.

[40] Sets 1 and 2 are used to analyze influences of density values for networks dominated by very long fractures

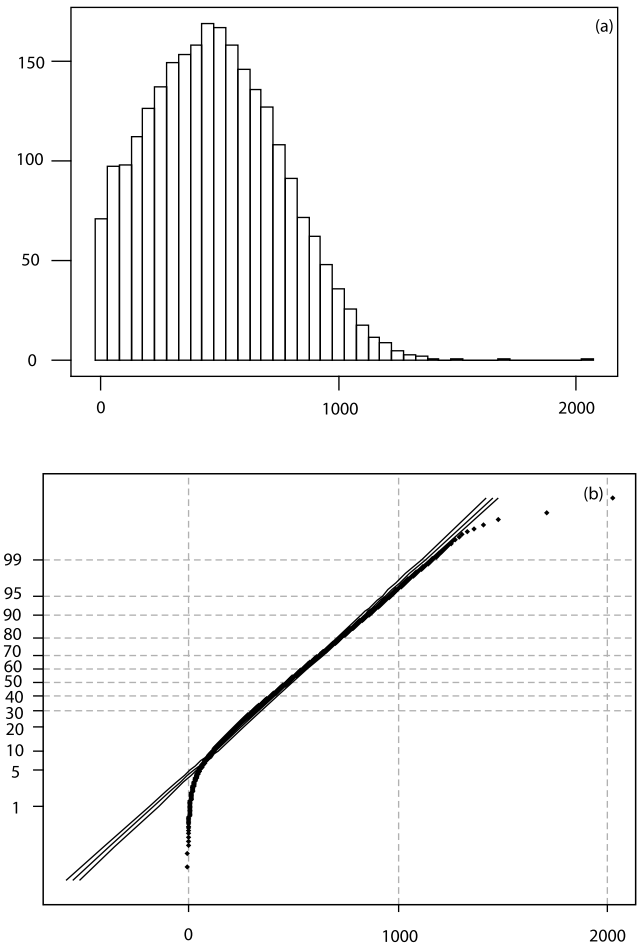

Figure 12. (a) Histogram and (b) Gaussian probability plot along Z_1 (longitudinal direction) of set 14 at a transport time of 100 years. The solid line represents a theoretical Gaussian trend along with upper and lower 95% confidence bounds. The deviation between the theoretical Gaussian trend and marginal particle displacements near the origin is attributed to anomalous subdiffusion (slow particle movement). Note also the heavier tail than the Gaussian trend at the leading edge. Approximately every 1/1000 point is plotted. Spatial values are given in units of meters.

(group 1, $1.0 \leq a \leq 1.6$). To test the hypothesis that truncation of particle pathways may lead to Fickian transport at very high spatial densities for group 1 networks, the spatial density value assigned to set 2 is well beyond the maximum density assigned to this distribution of fracture length exponents. When spatial density is dramatically increased from set 1 to set 2, the tail exponent estimates along Z_1 and Z_2 increase from 0.4–0.8 and 0.9–1.1 to 1.0–1.2 and 1.2–1.4, respectively (Figures 9 and 3). Higher tail estimates of α for set 2 are caused by the greater number of fractures that are connected to the hydraulic backbone within the release area. The release of particles into more fractures for set 2 leads to a greater sampling of fracture flow paths so that α values (α_1 = 1.0–1.2, α_2 = 1.2–1.4) more closely represent the distribution of fracture lengths (a_1 = 1.0, a_2 = 1.0). If truncation of fracture lengths was a controlling factor on transport rates, much higher tail estimates (i.e., closer to the finite variance threshold) would be expected because of the extremely high spatial density assigned to the network. Values of α based on plume spreading rates for set 2 match both tail estimates and fracture length exponent values. Therefore, convergence to an operator-stable density is much more likely in the highly fractured domain. The influence of density between sets 1 and 2 is also reflected in the timing and location of particles exiting model domain boundaries. For a total simulation time of 10,000 years, more than twice the number of particles leave the model domain boundary for set 2 because of the increased number of high-velocity pathways available for transport. The distribution of estimated mixing measure weights is unaffected by spatial density (not shown).

[41] The influence of density for fracture length exponent group 2 ($1.9 \leq a \leq 2.2$) on particle motion is observed in sets 9 and 10 where both a_1 and a_2 equal 1.9. Set 9 contains intermediate density values for both fracture groups, while set 10 contains a network where fracture groups contain minimum (Z_1) and maximum (Z_2) densities. Tails of marginal particle displacements for set 9 are power law with tail thickness estimates of 1.8–1.9. By increasing spatial density for one of the fracture groups in

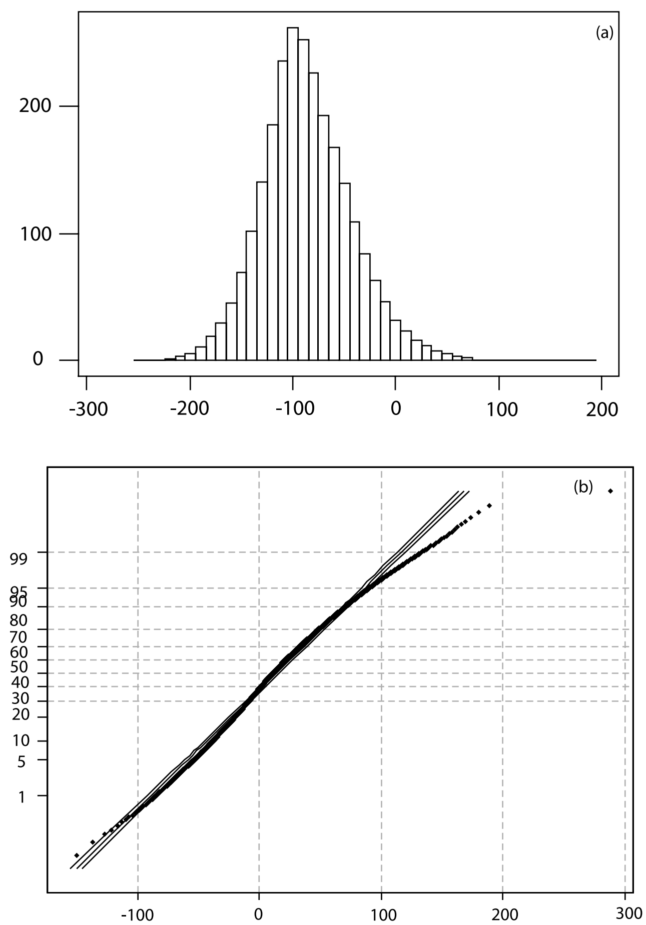

Figure 13. (a) Histogram and (b) Gaussian probability plot along Z_2 of set 14 at a transport time of 1000 years. The solid line represents a theoretical Gaussian trend along with upper and lower 95% confidence bounds. Spreading transverse to the ensemble plume is slighter heavier in both tails than a Gaussian. Approximately every 1/1000 point is plotted. Spatial values are given in units of meters.

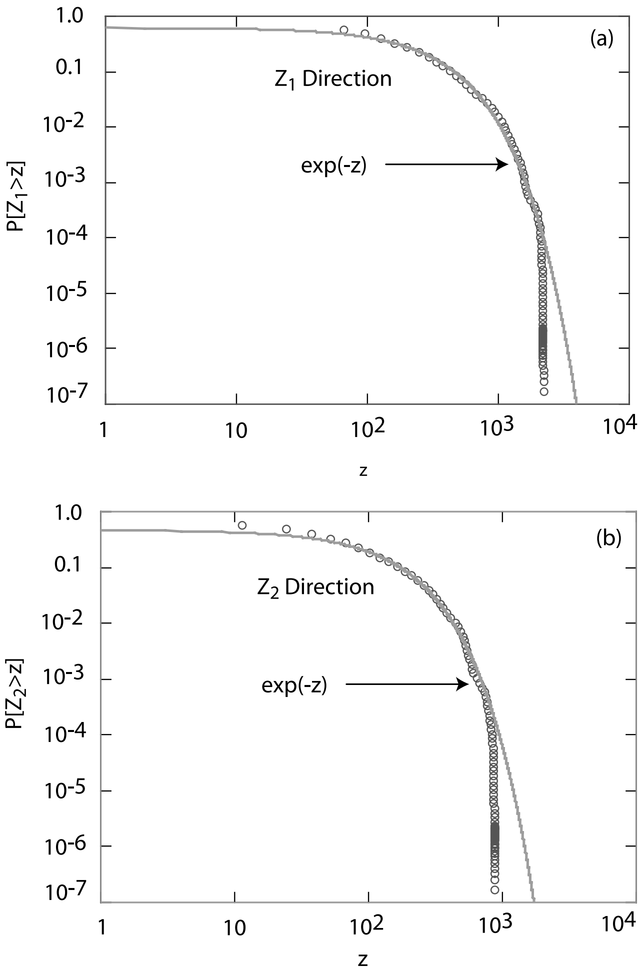

Figure 14. Mandelbrot plots of largest ranked particle displacements (circles) for set 13 along (a) Z_1 and (b) Z_2 with best fit exponential ($\exp(-z)$) trend at an elapsed time of 10^5 years. Approximately every 1/1000 point is plotted. Values of Z are given in units of meters.

parameter set 10, power law trends along both Z_1 and Z_2 are lost and the decay of the largest marginal particle displacements follows an exponential trend (Table 2). Regardless of tail behavior, the plume spreading rates for sets 9 and 10 are super-Fickian.

[42] Two pairs of parameter sets, sets 13–14 and sets 16–17, are used to investigate the influence of spatial density on solute transport for networks dominated by short fractures. These simulations show a general trend where spatial density controls the distribution of marginal particle displacements, the degree to which a plume spreads transverse to the hydraulic gradient, and transport times to model boundaries for group 3 networks. Compared to the more densely fractured networks (sets 14 and 17, Figure 2b), the networks with lower values of spatial density (sets 13 and 16, Figure 2a) lead to greater lateral spreading, exponential decay of marginal particle jumps (Figure 14), and longer particle arrival times to model boundaries.

[43] Increasing the network density from 0.27 m/m^2 in set 13 to 0.48 m/m^2 in set 14 results in Gaussian marginal displacement distributions (Figures 12 and 13) and decreases the time it takes the first particles to leave the down-gradient model boundary from 10,000 years (set 13) to 2154 years (set 14). A greater contrast in first particle arrival times to model boundaries (approximately two orders of magnitude decrease) is observed when the network density is increased from 0.30 m/m^2 for set 16 to 0.40 m/m^2 for set 17 as transport times to model boundaries decrease from 100,000 to 2154 years. Similar to set 14, Gaussian marginal displacement distributions were also observed for set 17 (not shown).

[44] While increases in fracture density were found to increase the mean network fluid flux by approximately an order of magnitude in both cases, the decrease in particle arrival time is primarily caused by the lack of transverse solute spreading. Lower spatial densities promote both a higher degree of spreading transverse to the hydraulic gradient and longer travel times to model boundaries, as lower spatial densities increase the tendency of particles to stay within individual fracture segments, allowing fracture orientation to exert more influence. At higher spatial densities, the intersection of individual fractures is enhanced, resulting in the truncation of pathways for solute migration and less transverse dispersion since more pathways aligned in the direction of the hydraulic gradient are available. This allows particles to move more rapidly toward the down-gradient model boundary.

3.4. Influence of Fracture Transmissivity

[45] Two substantially different probability density functions (pdfs) were selected to identify the role of the distribution of transmissivity values on ensemble solute transport rates. The primary transmissivity distribution is based on hydraulic testing on boreholes at the Äspo Hard Rock Laboratory, where transmissivity values recorded in 3 m intervals, match a Pareto distribution similar to (15) with a power law exponent of a_T = 0.4 along with minimum and maximum values of 10^{-11} and 10^{-2} m^2/s [*Gustafson and Fransson*, 2005]. For the same data, parameters for a lognormal distribution were estimated by forcing the data to a lognormal model resulting in a $\log_{10}(T)$ mean of -9.0 and standard deviation of 1.1. These values are very similar, especially in terms of standard deviation, to another hydraulic testing data set at Äspo Hard Rock Laboratory described by *Stigsson et al.* [2001] where the $\log_{10}(T)$ mean and standard deviation were estimated at -8.2 and 1.05, respectively. The truncated Pareto and lognormal (-9.0, 1.1) distributions are used to randomly assign fracture transmissivity to individual fractures. Fracture length and transmissivity are assumed uncorrelated.

[46] Four pairs of parameter sets, sets 3–4, 7–8, 14–15 and 18–19, are used to study the role of fracture transmissivity on particle transport rates. The first parameter set in each group assigns fracture transmissivity according to a truncated Pareto pdf (e.g., set 3), while the second parameter set assigns transmissivity using a lognormal pdf (e.g., set 4). With the exception of the transmissivity distribution, parameter sets and fracture realizations for each group are identical, even down to the random seed used to position the random number sequence.

[47] Estimates of α for sets 3 and 4 are almost identical for both tail and plume spreading methods. In the fracture

length discussion (section 3.2.1), we attributed the very heavy tailing observed for set 3 to both fracture length exponent values and a heavy-tailed distribution for fracture transmissivity. Set 4 indicates that this may only be partially correct. It is true that the very low fracture length exponent values (a_1 = 1.0, a_2 = 1.0) result in very long fractures that span the entire domain. Particles moving in these fractures are not influenced by other fractures so that fracture transmissivity governs the ensemble particle transport rates. However, both distributions allow transmissivity values to vary by orders of magnitude. Since particles traveling through only a few, very long fractures with high transmissivity values create the tail of the distribution, we hypothesize that for group 1 networks, heavy tails of marginal particle displacements can result from any transmissivity distribution that encompasses several orders of magnitude.

[48] The effect of different transmissivity distributions result in significant contrasts in tail estimates for sets 7 and 8 (a_1 = 1.6, a_2 = 2.2), though plume spreading rates and early particle arrival times are unaffected. While tail estimates for set 7 (Pareto-*T*) range between 1.2–1.6 and 1.9–exponential for Z_1 and Z_2, tail estimates for set 8 (lognormal-*T*) are significantly lower, 1.0–1.2 and 0.8–1.0. Particles first leave the model domain boundary at 10 years for both sets. Plume growth rates for both sets are very similar indicating that differences in tail estimates have little effect on overall plume growth. The major differences between the two parameter sets is demonstrated by the loss of particles at model domain boundaries. Over the course of 10,000 years, 2.5 times more particles leave the model domain for set 8 than for set 7. This is caused by the lognormal distribution having a higher median transmissivity than the truncated Pareto distribution. This effect was also observed for sets 18–19 where 20% more particles leave the model domain boundary for set 19 (lognormal-*T*). Upper tails of marginal particle displacements for sets 13–14 and 18–19 follow similar exponential and Gaussian probability decay trends, respectively.

3.5. Complex Networks

[49] Natural fracture networks typically consist of two [e.g., *LaPointe and Hudson*, 1985; *Barton*, 1995; *Ehlen*, 2000] or more fracture groups [e.g., *Billaux et al.*, 1989; *Gillespie et al.*, 1993; *Odling*, 1997] that cluster around distinct mean orientations. Fracture networks for sets 1–19 are restricted to two fracture groups with constant fracture orientation. Four additional parameter sets (sets 20–23) are used to evaluate more complex fracture networks. Fractures are allowed to deviate around mean orientations for sets 20, 21 and 23. Parameter sets 22 and 23 contain three fracture groups. Instead of investigating these influences over a wide range of fracture network statistics, we focus on network statistics that promote super-Fickian plume growth rates. This way the applicability of (5) to describe more complex ensemble particle displacement plumes as operator-stable densities is evaluated. Besides, previous simulations demonstrate that the convergence of ensemble particle displacements to symmetric, multi-Gaussian densities is limited to very dense networks with short fracture lengths.

[50] Deviations in fracture orientation about each mean are assigned according to a Fisher distribution [*Fisher*, 1953; *Butler*, 1992]:

$$f(\theta) = K\frac{\kappa \cdot e^{\kappa \cdot cos(\theta)}}{4\pi \sinh(\kappa)}, \tag{17}$$

where the deviation of fracture orientation from the mean, $-\frac{\pi}{2} < \theta < \frac{\pi}{2}$, is related to a dispersion parameter, κ. Low values of κ in (17) describe a large variability of fracture orientation from the mean, while large values indicate a tight clustering around the mean orientation (Figure 15). Values of κ for natural rock fractures range between 10 and 300 [*Kemeny and Post*, 2003; *Munier*, 2004]. A positive constant, *K*, ensures that $\int_{-\pi/2}^{\pi/2} f(\theta)d(\theta) = 1$. Since we use the rejection method [*Ross*, 1985] to generate Fisher random variables, *K* need not be computed explicitly.

[51] Sets 20 and 21 allow for deviations about two mean fracture orientations (based on fracture group orientations for set 1, $\theta_1 = 30°$, $\theta_2 = -60°$) according to Fisher dispersion parameters of $\kappa = 10$ and $\kappa = 50$, respectively. With the exception of variable fracture group orientations, sets 20 and 21 are identical to set 1 (Table 1), which is a very sparse network (ρ_{2D} = 0.015 m/m^2) with very long fracture lengths (a_1 = 1.0, a_2 = 1.0). Thus, variability in fracture orientation should have the most pronounced effect on these networks.

[52] As expected, plume growth directions for ensemble plumes for sets 20 and 21 are variable about the mean orientation, with more pronounced variability for the set with the lowest κ (Figure 16a). Since (17) symmetrically describes variability in fracture orientation about a mean orientation (Figure 15), we assume that eigenvector coordinates and mean fracture group orientations are correlated. Tail estimates of α for both sets 20 and 21 range 0.5–0.8 for Z_1 and 1.0–1.2 for Z_2, respectively. The range of α based on plume growth rates is narrow with estimates of 1.0–1.1 for each eigenvector. Estimates based on tail and plume growth methods are identical to results for set 1, indicating that deviations in fracture group orientation do not influence rates of particle transport. However, the influence of variability in fracture orientation for set 20 is reflected in both the observed and predicted distribution of mixing measure weights, where a greater variability of weights occurs along each eigenvector (Figure 7). The preferential movement of particles in fractures that are more favorably aligned in the direction of the mean hydraulic gradient cause a shift in mixing measure weights toward the mean down-gradient direction. This shift is more pronounced in the observed mixing measure weights computed from the ensemble particle displacement plumes (Figure 7b).

[53] Operator-stable densities for set 20, generated according to identical eigenvectors and eigenvalues, both illustrate the influence of the mixing measure on operator-stable densities and the utility of a multiscaling fractional advection-dispersion equation in describing highly irregular plumes (Figures 16b and 16c). The operator-stable density generated according to the observed mixing measure weights (Figure 16b) fails to capture the full degree of plume spreading observed in the ensemble displacement

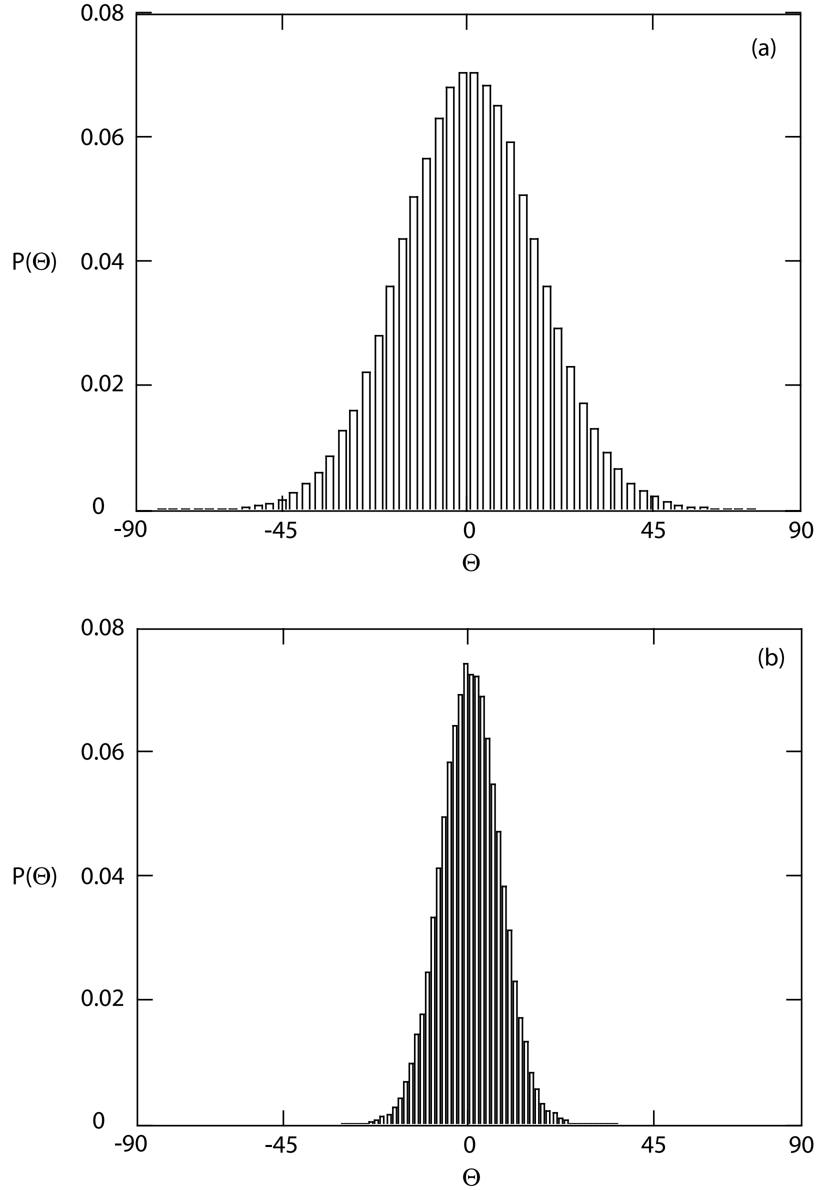

Figure 15. Probability histogram of 10^5 randomly generated Fisher deviates according to dispersion parameters of (a) κ = 10 and (b) κ = 50. Note the effect of κ on deviations about the mean, 0°.

plume (Figure 16a) and indicates that weights of the mixing measure are overestimated in the down-gradient direction. The operator-stable density based on the predicted mixing measure weights (Figure 16c) better captures the shape of the ensemble particle displacement plume, suggesting that this simple a priori method for computing mixing measure weights on the basis of mean ensemble fluid flux performs remarkably well.

[54] Networks for sets 22 and 23 contain three fracture groups oriented at ±45° and 90° with fracture length exponents of 1.6 and equal values of spatial density (ρ_{2D} = 0.025) for a total network density of 0.075 m/m^2. Fracture orientations for set 22 are constant, while fracture group orientations for set 23 are allowed to deviate according to a Fisher dispersion constant κ of 50. The orientation of the third fracture group (90°) relative to the hydraulic gradient is intended to investigate the role of a third fracture group on connectivity between the two fracture groups that are more preferably aligned with the hydraulic gradient.

[55] Ensemble particle displacement plumes (e.g., Figure 17a) confirm that the fracture group oriented at 90° does enhance connectivity (and solute mixing) between the other two fracture groups oriented at ±45° that are responsible for the majority of particle transport. However, a lower percentage of solute particles are transported normal to the gradient because of the combination of "pipe flow" methodology which propagates a regional gradient through all interconnected fractures regardless of orientation, and constant head conditions at all lateral boundaries. Since particle movement is two-dimensional, the two directions with the heaviest tails (lowest α values) are used to describe plume growth. This occurs along the fracture groups oriented at ±45°. Estimates of α based on both tail (0.9–1.2) and plume growth rate (1.1–1.3) methods are similar for both sets. However, the primary

difference between ensemble particle displacement plumes and an operator-stable density is the motion of particles via vertical transport in the fracture group oriented at 90° (Figure 17a). Both predicted and observed mixing measure weights did not account for particle motion in the vertical direction and the use of either of these mixing measure distributions results in an operator-stable density with symmetric growth along the eigenvectors (Figure 17b). By using mixing measure weights to describe a small amount of solute flux in the vertical direction, an operator-stable density can account for transport in the vertical direction (Figure 17c). This example demonstrates that predicted mixing measure weights must be adjusted to allow for a minimal amount of solute flux for fractures that are oriented orthogonal to a mean hydraulic gradient.

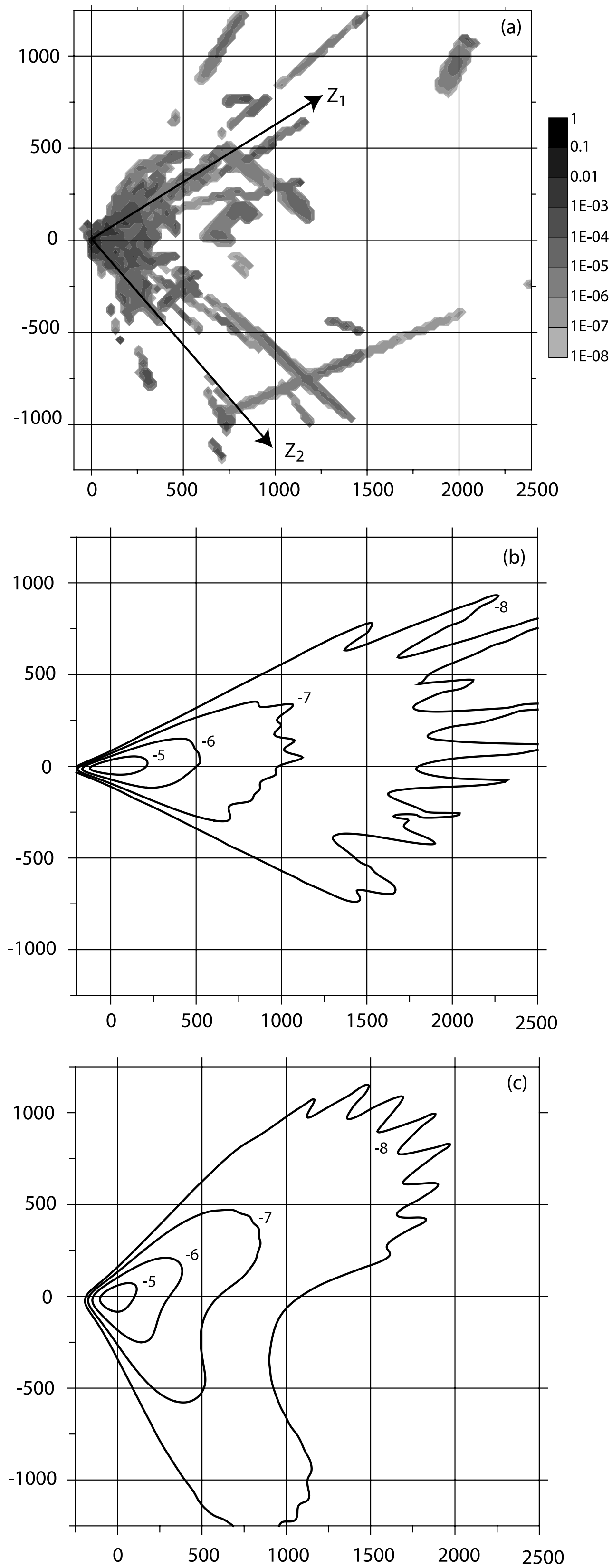

Figure 16. (a) Ensemble displacement plume for set 20 at a transport time of 10 years along with best fit operator-stable densities according to (b) observed and (c) predicted mixing measure weights. Note the influence of mixing measure on the geometry of the operator-stable densities shown in Figures 16b and 16c. The operator-stable density with predicted mixing measure weights better captures the spread observed in Figure 16a caused by the deviation in fracture orientation about the mean fracture groups, Z_1 and Z_2. All spatial values are given in units of meters. The pronounced "fingering" in the -8 contour is caused by multiple mixing measure directions. Contour intervals in Figures 16b and 16c are logarithmic.

4. Conclusion

[56] Data from fluid flow and particle-tracking simulations in networks with fractal length distributions demonstrate that ensemble particle displacement vectors have many characteristics of operator-stable densities including (1) power law tails of the largest particle displacements, (2) super-Fickian plume growth rates, (3) different growth rates in each coordinate, where coordinates correspond to the two main fracture orientations, and (4) nonelliptical plumes consistent with distinct (and discrete) directional measures describing plume shape. Particle motion in densely fractured domains with short fracture lengths result in roughly multi-Gaussian densities (an operator-stable subset) where elliptical plumes have, depending on values of fracture density, either exponential or Gaussian tailing. The motion process that describes the leading plume edges for particle displacement densities can be modeled using either integer-order or fractional-order ADEs, which describe ensemble transport according to a multi-Gaussian (a special case of operator stable) and operator-stable densities, respectively. However, the presence of particle retention in low-velocity segments of the hydraulic backbone was observed for all network types, and indicates that memory functions that govern the distribution of waiting times between particle jumps must be incorporated into the motion processes described by fractional-order and integer-order ADEs. This could be achieved by using either a continuous time random walk (CTRW) model [*Berkowitz and Scher*, 1997; *Scher et al.*, 2002; *Bijeljic and Blunt*, 2006] or a mobile-immobile model [*Schumer et al.*, 2003b; *Baeumer et al.*, 2005].

[57] Selection of a representative ADE to model the spatial transport characteristics of a fractured medium depends on transport regime. Quantifiable properties of the fractured medium, such as distributional properties of fracture length and values of spatial density, can be used to

distinguish between multi-Gaussian and operator-stable transport regimes (Figure 18). The transport regime is most heavily influenced by the distribution of fracture trace lengths, while spatial density plays a secondary role when fracture lengths are near, or just above, the finite variance threshold (a = 2). On the basis of comparisons between a heavy-tailed and thin-tailed transmissivity distribution, the distribution of fracture transmissivity does not significantly influence transport regime as long as fracture transmissivity is allowed to vary over several orders of magnitude.

[58] Operator-stable densities exclusively occur when power law fracture length exponent a is in the range $1.0 \leq a \leq 1.6$ even when spatial density values exceed natural limits. Although not specifically tested, this range most likely extends to $1.0 \leq a \leq 1.8$. For these network types, tail estimates of the operator-stable tail index α are lower than fracture length exponents and reflect the additional influence of a wide distribution of fracture transmissivity. Estimates of α based on plume spreading rates are higher than tail estimates and indicate ballistic transport where α is at, or slightly above, 1.0. Multi-Gaussian transport only occurs for networks when fracture lengths are in the range $2.5 \leq a \leq 3.0$ where the

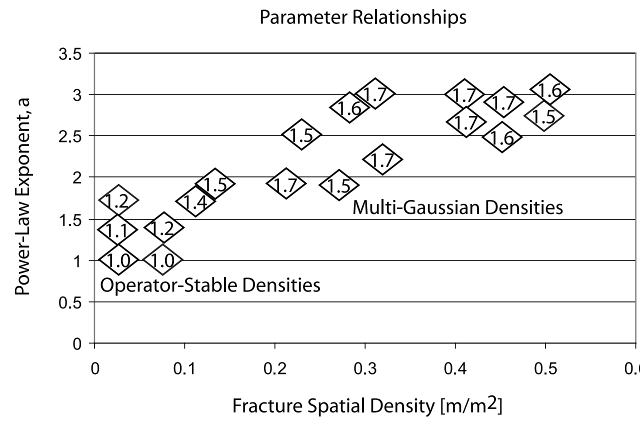

Figure 18. Correlation between fracture length exponent, fracture density, and resultant longitudinal plume growth rates (values of α inside diamonds) for individual fracture groups within sets 1–19. A clear threshold between operator-stable and multi-Gaussian transport regimes is not present. However, operator-stable transport regimes may be defined in fractured rock masses where individual fracture groups have fracture length exponent and density values less than 1.9 and 0.14 m/m^2, respectively. Note that particle retention results in super-Fickian plume growth rates (α < 2) for all network types.

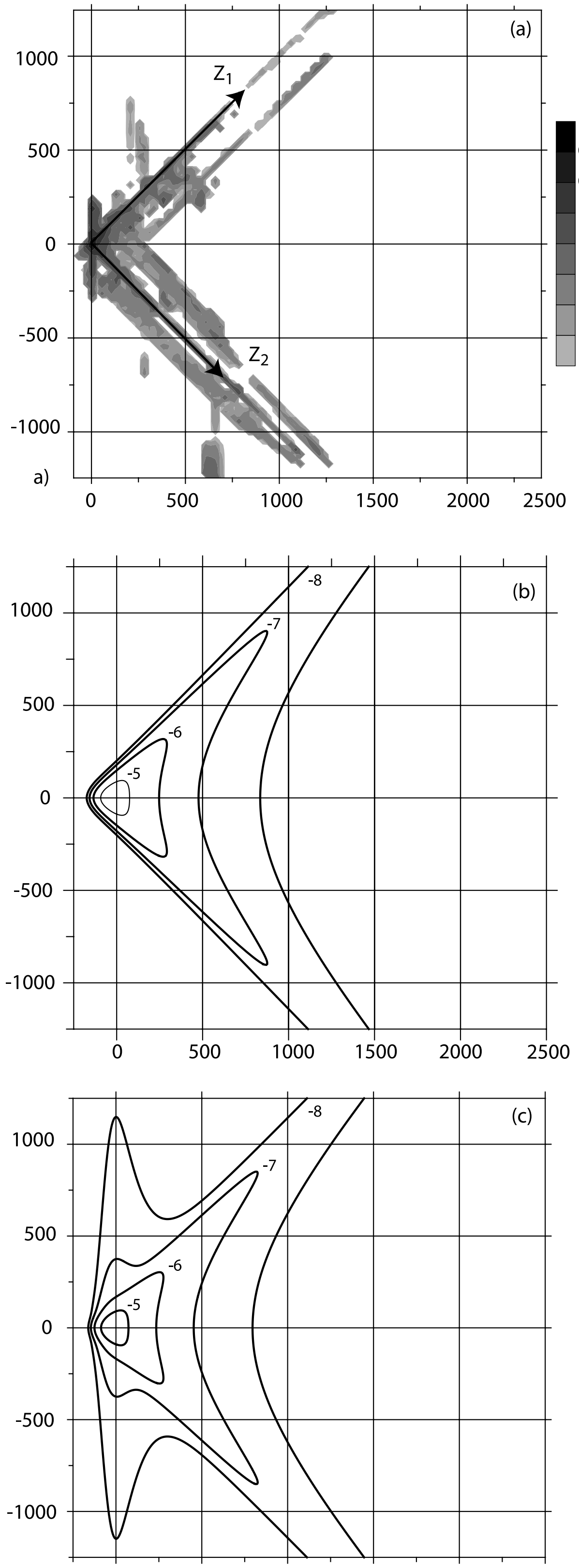

Figure 17. (a) Ensemble particle displacement plume for set 22 at a transport time of 100 years and (b and c) corresponding operator-stable densities based on ensemble plume characterization. An operator-stable density with mixing measure weights along the eigenvectors only (Figure 17b) is a good match for most of the ensemble plume but cannot adequately capture particle transport in the vertical fracture set. By allowing a small amount of solute flux in the vertical direction through the use of mixing measure weights, an operator-stable density (Figure 17c) can account for transport in the vertical fracture set. All spatial values are in meters. Contour intervals in Figures 17b and 17c are logarithmic.

combination of short fracture lengths and high fracture densities promote the formation of elliptical plumes with orthogonal growth directions. For shorter fracture lengths, values of spatial density exert a significant amount of control over particle arrival times at model boundaries and whether marginal particle displacements follow exponential or Gaussian trends. When the density is increased, with all other characteristics held constant, the likelihood of long segments in the transverse direction decreases; hence, particles move preferentially in the downstream direction, and particle arrivals at model boundaries can be up to two orders of magnitude faster.

[59] The threshold between multi-Gaussian and operator-stable transport regimes closely follows the boundary between infinite variance and finite variance distributions of fracture length. Moderately fractured networks with fracture lengths in the range $1.9 \leq a \leq 2.2$ can lead to marginal distributions of the largest particle displacements that can be either power law, Gaussian, or a combination of the two. For fracture groups where values of fracture length exponents equal 1.9, lower spatial densities ($\rho_{2D} < 0.14$ m/m^2) preserve the infinite variance nature of solute pathways resulting in power law tails, while higher spatial densities ($\rho_{2D} > 0.14$ m/m^2) result in the truncation of solute pathways and exponential probability decay at leading plume edges.

[60] Our findings demonstrate that the distribution of fracture length exerts a strong influence over solute movement in rock fracture networks, where unequal fracture length exponents for individual fracture groups can lead to plumes with dramatically different plume spreading rates along eigenvectors of plume growth. This is a departure from previous studies which only assign a single length exponent value to the entire network [*Renshaw*, 1999; *Zimmermann et al.*, 2003]. *Renshaw* [1999] proposed that fracture length exponent values for natural fracture networks are in the range $1.4 \leq a \leq 2.2$. This suggests that a super-Fickian model of transport such as the multiscaling fractional advection-dispersion equation may be applicable to more field sites than the conventional ADE, which has shown poor performance for sparsely fractured domains dominated by long fractures. The use of an analytical equation for solute transport predictions provides advantages over numerical simulations as less intensive field characterization is needed to produce screening-level predictions. In general, for operator-stable plumes eigenvectors correspond to principal fracture set orientations, power law fracture length exponent values provide a good estimate for values of α, and the distribution of mixing measure weights can be defined from the a priori method introduced in 3.1.2.2. This result implies that first-cut transport approximations for the leading plume edge in fractured media can be constructed from fracture network statistics. Significant differences between individual realizations call into question the assumption of an ergodic process. We investigate the goodness of fit between individual realizations and the ensemble in another paper (Reeves et al., submitted manuscript, 2007).

[61] **Acknowledgments.** This research was sponsored by grant DE-FG-02-07ER5841 from the Chemical Sciences, Geosciences, and Biosciences Division, Office of Basic Energy Sciences, Office of Science, U.S. Department of Energy, and by NSF grants DMS-0706440, DMS-0539176, EAR-9980489, and DMS-0139943; Desert Research Institute G.B. Maxey and NSF EPSCoR ACES fellowships; and the Marsden Fund, administered by the Royal Society of New Zealand. The DRI ACES supercomputer was essential for the numerical component of this research. We thank Eric LaBolle for making helpful modifications to his particle-tracking code.

References

Aban, I. B., M. M. Meerschaert, and A. K. Panorska (2006), Parameter estimation methods for the truncated Pareto distribution, *J. Am. Stat. Assoc.*, *101*, 270–277.

Baeumer, B., D. A. Benson, and M. M. Meerschaert (2005), Advection and dispersion in time and space, *Physica A*, *350*(2/4), 245–262.

Barton, C. C. (1995), Fractal analysis of scaling and spatial clustering of fractures, in *Fractals in the Earth Sciences*, edited by C. C. Barton and P. R. LaPointe, pp. 141–178, Plenum, New York.

Becker, M. W., and A. M. Shapiro (2000), Tracer transport in fractured crystalline rock: Evidence of non-diffusive breakthrough tailing, *Water Resour. Res.*, *36*(7), 1677–1686.

Benson, D. A. (1998), The fractional advection-dispersion equation: Development and application, Ph.D. thesis, Univ. of Nev., Reno.

Benson, D. A., S. W. Wheatcraft, and M. M. Meerschaert (2000), Application of a fractional advection-dispersion equation, *Water Resour. Res.*, *36*(6), 1403–1412.

Berkowitz, B., and H. Scher (1995), On the characterization of anomalous dispersion in porous and fractured media, *Water Resour. Res.*, *31*(6), 1461–1466.

Berkowitz, B., and H. Scher (1997), Anomalous transport in random fracture networks, *Phys. Rev. Lett.*, *79*(20), 4038–4041.

Bijeljic, B., and M. J. Blunt (2006), Pore-scale modeling and continuous time random walk analysis of dispersion in porous media, *Water Resour. Res.*, *42*, W01202, doi:10.1029/2005WR004578.

Billaux, D. M., J. P. Chiles, and C. Hestir (1989), Three-dimensional statistical modelling of a fractured rock mass—An example from the Fanay-Augères Mine, *Int. J. Rock Mech. Min. Sci. Geomech. Abstr.*, *36*(3–4), 281–299.

Bingham, C. (1964), Distributions on the sphere and on the projective plane, Ph.D. dissertation, Yale Univ., New Haven, Conn.

Bonnet, E., O. Bour, N. E. Odling, P. Davy, I. Main, P. Cowie, and B. Berkowitz (2001), Scaling of fracture systems in geologic media, *Rev. Geophys.*, *39*(3), 347–383.

Bour, O., and P. Davy (1997), Connectivity of random fault networks following a power law fault length distribution, *Water Resour. Res.*, *33*(7), 1567–1583.

Butler, R. F. (1992), *Paleomagnetism: Magnetic Domains to Geologic Terranes*, Blackwell Sci., Oxford, U. K.

Carr, J. R. (2002), *Data Visualization in the Geosciences*, Prentice-Hill, Upper Saddle River, N. J.

de Dreuzy, J.-R., P. Davy, and O. Bour (2001), Hydraulic properties of two-dimensional random fracture networks follwing a power law length distribution: 1. Effective connectivity, *Water Resour. Res.*, *37*(8), 2065–2078.

Dentz, M., and B. Berkowitz (2003), Transport behavior of a passive solute in continuous time random walks and multirate mass transfer, *Water Resour. Res.*, *39*(5), 1111, doi:10.1029/2001WR001163.

Ehlen, J. (2000), Fractal analysis of joint patterns in granite, *Int. J. Rock Mech. Min. Sci.*, *37*, 909–922.

Fisher, R. (1953), Dispersion on a sphere, *Proc. R. Soc. London, Ser. A*, *217*, 295–305.

Follin, S., and R. Thunvik (1994), On the use of continuum approximations for regional modeling of groundwater flow through crystalline rocks, *Adv. Water Resour.*, *17*, 133–145.

Gillespie, P. A., C. B. Howard, J. J. Walsh, and J. Watterson (1993), Measurement and characterization of spatial distributions of fractures, *Tectonophysics*, *226*, 113–141.

Gustafson, G., and A. Fransson (2005), The use of the Pareto distribution for fracture transmissivity assessment, *Hydrogeol. J.*, *14*, 15–20, doi:10.1007/s10040-005-0440-y.

Haggerty, R., and S. M. Gorelick (1995), Multiple-rate mass transfer for modeling diffusion and surface reactions in media with pore-scale heterogeneity, *Water Resour. Res.*, *31*(10), 2383–2400.

Haggerty, R., S. A. McKenna, and L. C. Meigs (2000), On the late-time behavior of tracer test breakthrough curves, *Water Resour. Res.*, *36*(12), 3467–3479.

Jiménez-Hornero, J., V. Giráldez, A. Laguna, and Y. Pachepsky (2005), Continuous time random walks for analyzing the transport of a passive tracer in a single fissure, *Water Resour. Res.*, *41*, W04009, doi:10.1029/2004WR003852.

Jurek, Z. J. (1984), Polar coordinates in Banach spaces, *Bull. Acad. Pol. Math.*, *32*, 61–66.

Kemeny, J., and R. Post (2003), Estimating three-dimensional rock discontinuity orientation from digital images of fracture traces, *Comput. Geosci.*, *29*, 65–77.

Kosakowski, G. (2004), Anomalous transport of colloids and solutes in a shear zone, *J. Contam. Hydrol.*, *72*, 23–46.

LaPointe, P. R., and J. A. Hudson (1985), Characterization and interpretation of rock mass joint patterns, *Geol. Soc. Am. Spec. Pap.*, *199*.

Long, J. C. S., J. S. Remer, C. R. Wilson, and P. A. Witherspoon (1982), Porous media equivalent for networks of discontinuous fractures, *Water Resour. Res.*, *18*(3), 645–658.

Meerschaert, M. M., and H. P. Scheffler (2001), *Limit Distributions for Sums of Independent Random Vectors: Heavy Tails in Theory and Practice*, John Wiley, New York.

Meerschaert, M. M., and H. P. Scheffler (2003), Nonparametric methods for heavy tailed vector data: A survey with applicatons from finance to hydrology, in *Recent Advances and Trends in Nonparametric Statistics*, edited by M. G. Akritas and D. N. Politis, pp. 256–279, Elsevier Sci., Amsterdam.

Meerschaert, M. M., D. A. Benson, and B. Baeumer (1999), Multidimensional advection and fractional dispersion, *Phys. Rev. E*, *59*, 5026–5028.

Meerschaert, M. M., D. A. Benson, and B. Baeumer (2001), Operator Lévy motion and multiscaling anomalous diffusion, *Phys. Rev. E*, *63*, 021112.

Mercado, A. (1967), The spreading pattern of injected water in a permeability-statified aquifer, *IAHS AISH Publ.*, *72*, 23–36.

Munier, R. (2004), Statistical analysis of fracture data adapted for modelling discrete fracture networks version 2, *Rep. R 04–66*, Swed. Nucl. Fuel and Waste Manage., Stockholm.

Odling, N. (1997), Scaling and connectivity of joint systems in sandstones from western Norway, *J. Struct. Geol.*, *19*, 1257–1271.

Painter, S., V. Cvetkovic, and J. Selroos (2002), Power-law velocity distributions in fracture networks: Numerical evidence and implications for tracer transport, *Geophys. Res. Lett.*, *29*(14), 1676, doi:10.1029/2002GL014960.

Reeves, D. M., D. A. Benson, and M. M. Meerschaert (2008), Transport of conservative solutes in simulated fracture networks: 1. Synthetic data generation, *Water Resour. Res.*, doi:10.1029/2007WR006069, in press.

Renshaw, C. E. (1997), Mechanical controls on the spatial density of opening-mode networks, *Geology*, *25*(10), 923–926.

Renshaw, C. E. (1999), Connectivity of joint networks with power law length distributions, *Water Resour. Res.*, *35*(9), 2661–2670.

Ross, S. M. (1985), *Introduction to Probability Models*, 3rd ed., Academic, Orlando, Fla.

Scheffler, H.-P. (1999), On estimation of the spectral measure of certain nonnormal operator stable laws, *Stat. Probab. Lett.*, *43*, 385–392.

Scher, H., G. Margolin, and B. Berkowitz (2002), Towards a unified framework for anomalous transport in heterogeneous media, *Chem. Phys.*, *284*, 349–359.

Schumer, R., D. A. Benson, M. M. Meerschaert, and B. Baeumer (2003a), Multiscaling fractional advection-dispersion equations and their solutions, *Water Resour. Res.*, *39*(1), 1022, doi:10.1029/2001WR001229.

Schumer, R., D. A. Benson, M. M. Meerschaert, and B. Baeumer (2003b), Fractal mobile/immobile solute transport, *Water Resour. Res.*, *39*(10), 1296, doi:10.1029/2003WR002141.

Schwartz, F. W., L. Smith, and A. S. Crowe (1983), A stochastic analysis of macroscopic dispersion in fractured media, *Water Resour. Res.*, *19*(5), 1253–1265.

Smith, L., and F. W. Schwartz (1984), An analysis on the influence of fracture geometry on mass transport in fractured media, *Water Resour. Res.*, *20*(9), 1241–1252.

Stigsson, M., N. Outters, and J. Hermanson (2001), Äspö Hard Rock Laboratory, prototype repository hydraulic DFN model 2, *Int. Prog. Rep. IPR 01-39*, Swed. Nucl. Fuel and Waste Manage., Stockholm.

Strang, G. (1988), *Linear Algebra and its Applications*, 3rd ed., Harcourt, New York.

Zhang, D., and Q. Kang (2004), Pore scale simulation of solute transport in fractured porous media, *Geophys. Res. Lett.*, *31*, L12504, doi:10.1029/2004GL019886.

Zimmermann, G., H. Burkhardt, and L. Engelhard (2003), Scale dependence of hydraulic and structural parameters in the crystalline rock of the KTB, *Pure Appl. Geophys.*, *160*, 1067–1085.

D. A. Benson, Department of Geology and Geological Engineering, Colorado School of Mines, 1500 Illinois Street, Golden, CO 80401, USA. (dbenson@mines.edu)

M. M. Meerschaert, Department of Statistics and Probability, Michigan State University, A413 Wells Hall, East Lansing, MI 48823, USA. (mcubed@stt.msu.edu)

D. M. Reeves, Desert Research Institute, 2215 Raggio Parkway, Reno, NV 89512, USA. (mreeves@dri.edu)

H.-P. Scheffler, Department of Mathematics, University of Siegen, D-57068 Siegen, Germany. (scheffler@mathematik.uni-siegen.de)